ELSEVIER

Mars atmospheric chemistry simulations with the GEM-Mars general circulation model

F. Daerden[a,*], L. Neary[a], S. Viscardy[a], A. García Muñoz[b], R.T. Clancy[c], M.D. Smith[d], T. Encrenaz[e], A. Fedorova[f]

[a] Royal Belgian Institute for Space Aeronomy BIRA-IASB, Brussels, Belgium
[b] Zentrum für Astronomie und Astrophysik, Technische Universität Berlin, Berlin, Germany
[c] Space Science Institute, Boulder, CO, USA
[d] NASA Goddard Space Flight Center, Greenbelt, MD, USA
[e] LESIA, Observatoire de Paris, CNRS, UPMC, UPD, Meudon, France
[f] Space Research Institute (IKI), RAS, Moscow, Russian Federation

ARTICLE INFO

ABSTRACT

General Circulation Models with interactive physical and chemistry processes are the state-of-the-art tools for an integrated view and understanding of the Martian atmosphere and climate system. The GEM-Mars model currently includes 16 tracers for chemical composition and applies a fully online, interactive calculation of the photo- and gas phase chemistry of carbon dioxide (CO_2) and water vapor (H_2O). These species largely control the chemical composition of the neutral Mars atmosphere through their photolysis products and their subsequent interactions. Water vapor undergoes a complex cycle on Mars as it is transported and interacts with ice reservoirs both at the planet's surface and at water ice clouds, which in turn provide radiative feedbacks. In the photochemical cycles involving CO_2 and H_2O, the abundances of 5 species have been reported by previous investigations with significant spatio-temporal coverage: CO_2, H_2O, CO, O_3 and H_2O_2. This paper presents the current status of the atmospheric chemistry simulations in GEM-Mars by comparing them to a selection of these observational datasets as well as to oxygen dayglow emission from $O_2(a^1\Delta_g)$. The results are consistent with previous model-data comparisons and illustrate that the water cycle and the photochemistry are well implemented in the model. In particular, the simulation of the key reservoir species H_2O_2 provides a good match to the available data. Model-data biases for ozone columns and oxygen airglow are related to the simulated water vapor vertical profile, as these species have important column contributions from vertical layers at the top of the hygropause.

1. Introduction

The chemical composition of the atmosphere of Mars has been a long-standing topic of research, ever since the pioneering work of e.g. Kuiper (1949), Spinrad et al. (1963), Kaplan et al. (1969), Barker (1972), Carleton and Traub (1972), and the early space age investigations, e.g., Barth and Hord (1971), Owen et al. (1977), Jakosky and Farmer (1982). The nearly continuous monitoring of the Martian atmosphere since 1999 by the NASA's Mars Global Surveyor (MGS), Mars Odyssey (MOD) and Mars Reconnaissance Orbiter (MRO), and ESA's Mars Express (MEX) missions, together with an increased set of Earth-based observations, have greatly refined the picture. In-situ measurements of the relative (near-surface) abundances of the major constituents were provided by NASA's Mars Science Laboratory's (MSL)

Tunable Laser Spectrometer/Sample Analysis at Mars (TLS-SAM) suite: CO_2 (volume mixing ratio, vmr): 0.957 ± 0.016, Ar: 0.0207 ± 0.0002, N_2: 0.0203 ± 0.0003, O_2: $(1.73 \pm 0.06) \times 10^{-3}$, and CO: $(7.49 \pm 0.026) \times 10^{-4}$ (Franz et al., 2015). Several of the remaining minor constituents were measured from orbit and from Earth: H_2O (e.g. Smith, 2004; Smith et al., 2018, Fedorova et al. (2006)), HDO (e.g. Villanueva et al., 2015; Aoki et al., 2015a, 2015b; Encrenaz et al., 2016; 2018), O_3 (e.g. Perrier et al., 2006; Clancy et al., 2016), H_2O_2 (e.g. Clancy et al., 2004; Encrenaz et al., 2004, 2012, 2015), and OH (Clancy et al., 2013). For a more exhaustive description and more references, see Haberle et al. (2017).

The picture that was developed in photochemical models (e.g. Moreau et al., 1991; Krasnopolsky, 1993; Nair et al., 1994; Lefèvre et al., 2004; García Muñoz et al., 2005) and that is supported by the

---

* Corresponding author.
  E-mail address: Frank.Daerden@aeronomie.be (F. Daerden).

observations is that of an oxidized atmosphere that is chemically controlled by CO_2 and H_2O and their photolysis products and their subsequent interactions. A deviation from this may be the reported detection of methane (CH_4, e.g. Mumma et al., 2009; Webster et al., 2015, 2018, and references therein), which is chemically not stable on Mars (Summers et al., 2002; Zahnle et al., 2011) so its detection implies recent formation or release. The detections of methane as well as their interpretation are not yet fully understood, but they triggered new research for possible active processes. This revived the old idea of Hitchcock and Lovelock (1967) that Life on Mars could be detected by signatures of disequilibria in the atmosphere, but methane may also result from geochemical and related processes (e.g. Atreya et al., 2007; Oehler and Etiope, 2017; Etiope, 2018). It added to the inspiration for the concept of the ESA-Roskosmos ExoMars Trace Gas Orbiter (TGO) mission (Zurek et al., 2011) that is now in orbit around Mars, and that was designed to improve the current detection limit of minor species by more than an order of magnitude, with special high sensitivity for methane (Vandaele et al., 2015, 2018; Korablev et al., 2015, 2018). But TGO has a much wider potential than methane detection, including the first highly resolved vertical profiles of water vapor, HDO, carbon monoxide, and many other species (Vandaele et al., 2015), and is expected to significantly extend our knowledge about the atmospheric composition of Mars.

1.1. Global models for Mars atmospheric chemistry

Following similar developments in Earth atmospheric research, three-dimensional models for the chemistry in the atmosphere of Mars were developed more than a decade ago (Lefèvre et al., 2004; Moudden and McConnell, 2007). A 3D model that simulates the circulation and dynamics of a planetary atmosphere is called a General Circulation Model (GCM, sometimes also called a Global Climate Model). In the case of Earth, atmospheric chemistry was rather simulated in 3D Chemical Transport Models (CTMs, e.g. Chipperfield et al., 1993; Lefèvre et al., 1994; Daerden et al., 2007), in which chemical tracers are passively advected and undergo chemical reactions using preexisting 3D dynamical fields (called *analyses*). The latter are provided by meteorological centers that possess huge computing machines that can integrate the vast information from weather stations and satellites into the GCMs using the technique of data assimilation (e.g. Talagrand, 1997; Kalnay, 2003).

There is some apparent contradiction in this respect, as on Earth, the radiative feedback of the chemical composition on the dynamics is actually very large, notably for O_3 (causing the temperature inversion and the existence of the stratosphere) and greenhouse gases. However, because of the accurate dynamical analyses, this poses no real problem for CTM studies. On Mars, with an atmospheric pressure of over 2 orders lower than on Earth, the greenhouse effect is very weak (e.g. Savijärvi et al., 2004), while the ozone abundances are typically 3 orders of magnitude less than on Earth (e.g. Montmessin and Lefèvre, 2013). But the impact of water vapor, notably through radiative feedbacks by water ice clouds (e.g. Madeleine et al., 2012) and surface ice, is very strong. This process is complicated, because cloud formation depends on the temperature, which is then modified by the clouds, a sensitive balance that ideally requires detailed microphysical models (Navarro et al., 2014a; Spiga et al., 2017).

While data assimilation systems for Mars are being developed (e.g. Lewis et al., 2007; Greybush et al., 2012; Steele et al., 2014a, 2014b; Navarro et al., 2014b), the datasets for the vertical distribution of water vapor are not dense and resolved enough yet (Maltagliati et al. (2011, 2013), Clancy et al. (2017), and Fedorova et al. (2018)) to provide a coverage and quality of analysis similar to that on Earth. So on Mars, the simulation of atmospheric chemistry necessarily has to go hand in hand with the development of the dynamical models in order to provide self-consistent simulations. As a result, the simulated chemistry can only be as accurate as allowed for by the resolved physical and

dynamical processes. The TGO mission is expected to strongly improve our knowledge of the water vapor vertical distribution on Mars (Vandaele et al., 2015, 2018; Korablev et al., 2015, 2018).
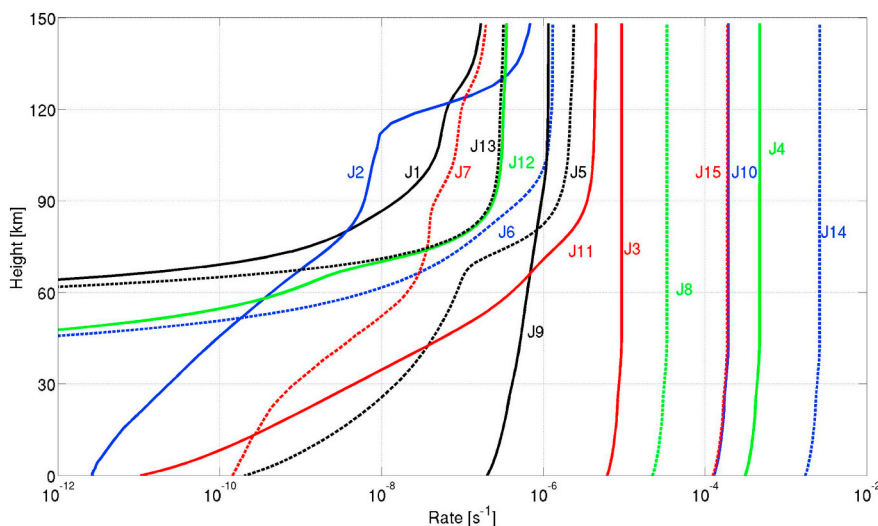
Table 1

List of photolysis and radiative decay reactions in GEM-Mars. Rates are taken from García Muñoz et al. (2005). An example of the rates is given in Fig. 1.

Label	Reaction
J1	$CO_2 + h\nu \rightarrow CO + O(^1D)$
J2	$CO_2 + h\nu \rightarrow CO + O$
J3	$O_3 + h\nu \rightarrow O_2 + O(^1D)$
J4	$O_3 + h\nu \rightarrow O_2 + O$
J5	$O_3 + h\nu \rightarrow 3\,O$
J6	$O_2 + h\nu \rightarrow O + O(^1D)$
J7	$O_2 + h\nu \rightarrow 2\,O$
J8	$H_2O_2 + h\nu \rightarrow 2\,OH$
J9	$H_2O_2 + h\nu \rightarrow HO_2 + H$
J10	$HO_2 + h\nu \rightarrow OH + O$
J11	$H_2O + h\nu \rightarrow H + OH$
J12	$H_2O + h\nu \rightarrow H_2 + O(^1D)$
J13	$H_2O + h\nu \rightarrow 2H + O$
J14	$O_3 + h\nu \rightarrow O_2(a^1\Delta_g) + O(^1D)$
J15	$O_2(a^1\Delta_g) \rightarrow O_2 + h\nu\ (1.27\,\mu m)$

Table 2

List of gas-phase reactions in GEM-Mars. R1–22 are 2-body reactions, R23–29 are 3-body reactions with CO_2 as 3rd body, and R30–31 relate to oxygen airglow. The unit of the rate coefficient for 2-body reactions is $cm^3\,s^{-1}$ and for 3-body reactions $cm^6\,s^{-1}$. All rate coefficients are taken from García Muñoz et al. (2005), except R30 which was reduced following Clancy et al. (2017). An example of the rate coefficients is given in Fig. 2.

Label	Reaction	Rate coefficient
Two body reactions		
R1	$CO + OH \rightarrow CO_2 + H$	1.5×10^{-13}
R2	$O + O_3 \rightarrow 2\,O_2$	$8.0 \times 10^{-12} \times exp.(-2060/T)$
R3	$O(^1D) + CO_2 \rightarrow O + CO_2$	$7.4 \times 10^{-11} \times exp.(120/T)$
R4	$O(^1D) + H_2 \rightarrow OH + H$	1.1×10^{-10}
R5	$O(^1D) + H_2O \rightarrow 2\,OH$	2.2×10^{-10}
R6	$O(^1D) + O_3 \rightarrow 2\,O_2$	1.2×10^{-10}
R7	$O(^1D) + O_3 \rightarrow O_2 + 2\,O$	1.2×10^{-10}
R8	$O(^1D) + O_2 \rightarrow O + O_2$	$3.2 \times 10^{-11} \times exp.(70/T)$
R9	$H + O_3 \rightarrow OH + O_2$	$1.4 \times 10^{-10} \times exp.(-470/T)$
R10	$O + OH \rightarrow O_2 + H$	$2.2 \times 10^{-11} \times exp.(120/T)$
R11	$O + HO_2 \rightarrow OH + O_2$	$3.0 \times 10^{-11} \times exp.(200/T)$
R12	$HO_2 + OH \rightarrow H_2O + O_2$	$4.8 \times 10^{-11} \times exp.(250/T)$
R13	$H + HO_2 \rightarrow H_2 + O_2$	6.48×10^{-12}
R14	$H + HO_2 \rightarrow H_2O + O$	1.62×10^{-12}
R15	$H + HO_2 \rightarrow 2\,OH$	7.29×10^{-11}
R16	$2\,HO_2 \rightarrow H_2O_2 + O_2$	$2.3 \times 10^{-13} \times exp.(600/T)$
R17	$O + H_2O_2 \rightarrow OH + HO_2$	$1.4 \times 10^{-12} \times exp.(-2000/T)$
R18	$HO_2 + O_3 \rightarrow OH + 2\,O_2$	$1.0 \times 10^{-14} \times exp.(-490/T)$
R19	$H_2 + OH \rightarrow H + H_2O$	$5.5 \times 10^{-12} \times exp.(-2000/T)$
R20	$H_2O_2 + OH \rightarrow HO_2 + H_2O$	$2.9 \times 10^{-12} \times exp.(-160/T)$
R21	$OH + O_3 \rightarrow HO_2 + O_2$	$1.7 \times 10^{-12} \times exp.(-940/T)$
R22	$2\,OH \rightarrow H_2O + O$	$4.2 \times 10^{-12} \times exp.(-240/T)$
Three body reactions		
R23	$CO + O + CO_2 \rightarrow 2\,CO_2$	$5.92 \times 10^{-33} \times exp.(-2031.4/T)$
R24	$O + O_2 + CO_2 \rightarrow O_3 + CO_2$	$1.216 \times 10^{-27} \times T^{-2.4}$
R25	$2\,O + CO_2 \rightarrow O_2 + CO_2$	$8.16 \times 10^{-35} \times exp.(900/T)$
R26	$H + O_2 + CO_2 \rightarrow HO_2 + CO_2$	$1.205 \times 10^{-27} \times T^{-1.6}$
R27	$2\,OH + CO_2 \rightarrow H_2O_2 + CO_2$	$4.76 \times 10^{-28} \times T^{-1}$
R28	$2H + CO_2 \rightarrow H_2 + CO_2$	$2.7 \times 10^{-31} \times T^{-0.6}$
R29	$2\,HO_2 + CO_2 \rightarrow H_2O_2 + O_2 + CO_2$	$3.91 \times 10^{-33} \times exp.(1000/T)$
Airglow related reactions		
R30	$O_2(a^1\Delta_g) + CO_2 \rightarrow O_2 + CO_2$	0.25×10^{-20}
R31	$2\,O + CO_2 \rightarrow O_2(a^1\Delta_g) + CO_2$	$1.59 \times 10^{-34} \times exp.(900/T)$

Fig. 1. Photolysis rates of reactions in Table 1, for solstice ($L_s = 90°$) at latitude 40°, longitude 0°, local time is noon, solar zenith angle (SZA) is 15°.
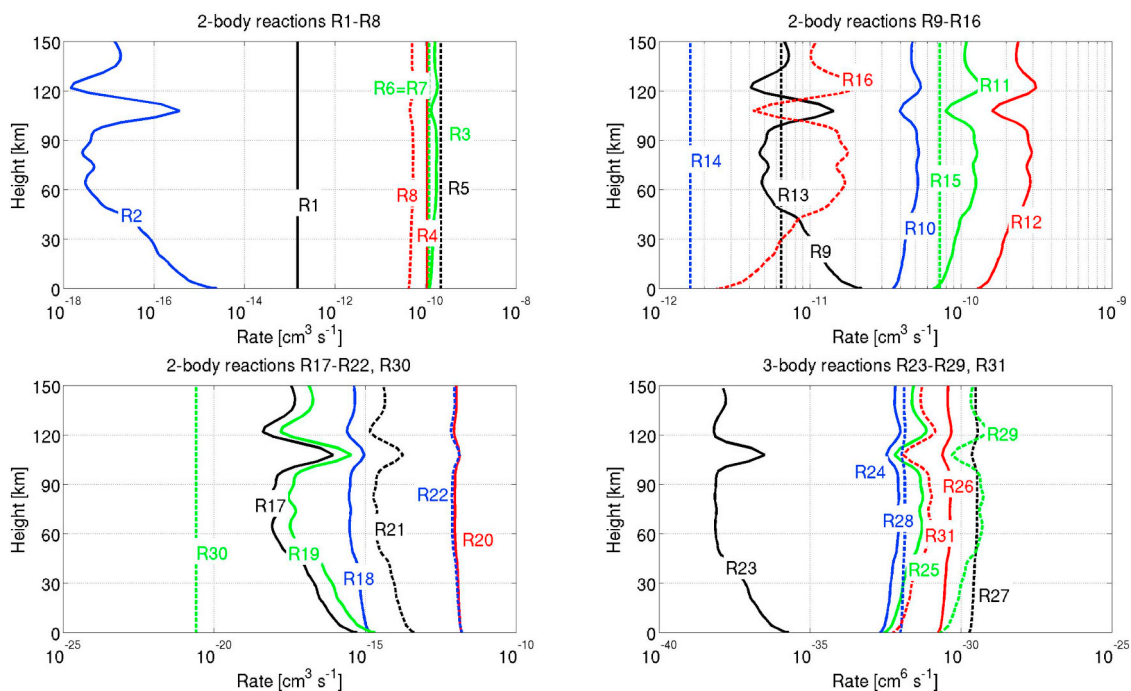

Fig. 2. Rate coefficients of reactions in Table 2, for the same conditions as in Fig. 1. Rate coefficients have been distributed over several frames for better visibility.

1.2. The GEM-Mars model

Until present two Mars GCMs with atmospheric chemistry have been developed: the model of the Laboratoire de Météorologie Dynamique (hereafter LMD model) and the Global Environmental Multiscale or GEM model. Of these, the LMD model (Lefèvre et al., 2004) has by far been the most applied and evaluated model (e.g. Perrier et al., 2006; Lebonnois et al., 2006; Fedorova et al., 2006; Lefèvre et al., 2008; Gagné et al., 2012; Montmessin and Lefèvre, 2013; Encrenaz et al., 2015; Clancy et al., 2012, 2013, 2016, 2017). The same chemical routines were also implemented and applied in the UK version of the LMD model (Holmes et al., 2017). The GEM model was developed by the Recherche en Prévision Numérique (RPN) division of Environment Canada (Côté et al., 1998a, 1998b; Yeh et al., 2002) for weather forecasting on Earth. It was first accommodated for Mars in the GM3 model of Moudden and McConnell (2005), that was applied to study Mars atmospheric chemistry in Moudden and McConnell (2007).

Later on, the development of the Mars version of this model diverged in two directions. The University of Colorado focused on applying the GM3 model on the study of waves and tides in the Martian atmosphere (Moudden and Forbes, 2008a, 2008b, 2014, 2015). At York University GM3 was applied for studies of the water cycle (Akingunola, 2008), dust lifting (Wu, 2015) and south polar meteorology (Fazel-Rastgar, 2016). York University also started a collaboration with the Royal Belgian Institute for Space Aeronomy (BIRA-IASB) to extend and refine the physical parameterizations of the Mars model and to further develop the atmospheric chemistry routines. The involved chemical processes were based on those in García Muñoz et al. (2005) but with an implementation that stayed closer to that of the GEM-AQ model, that was developed for atmospheric chemistry and air quality (AQ) on Earth (Kaminski et al., 2008). For this reason, the model was renamed to GEM-Mars (with the option to develop GEM type of models for other planets or applications). At BIRA-IASB the model was adapted to the GEM 4.2.0 version of the mother model, which is one of the more recent
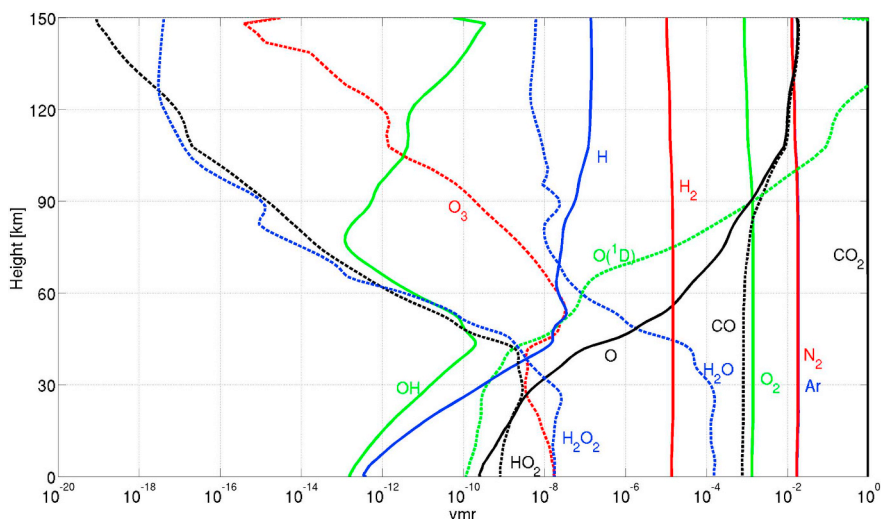
Fig. 3. Vertical profiles of the vmr of the species simulated in the model at the time and location of Figs. 1 and 2.
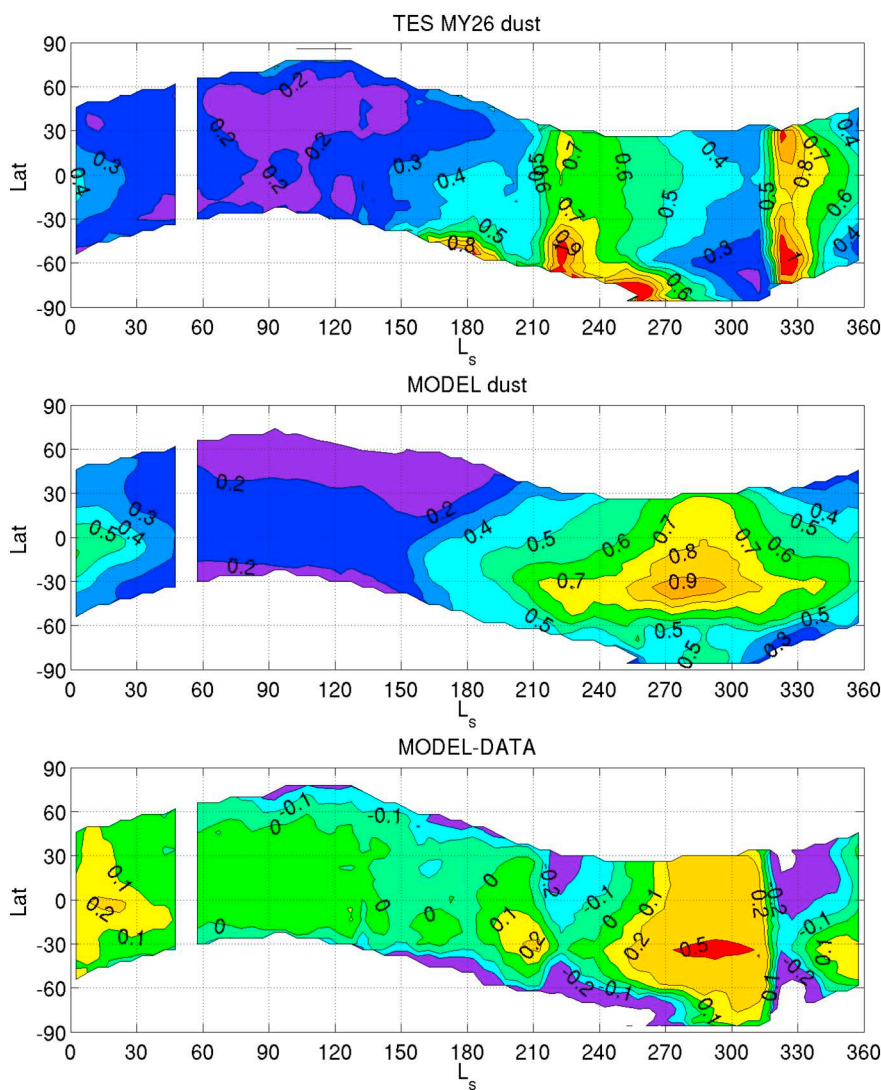

Fig. 4. Seasonal and latitudinal variation of the visible dust optical depth observed by TES in Mars year 26 (top) and simulated in the model (middle), and their difference (bottom). The model results are for daytime conditions (1–3 p.m., SZA < 80°). Data and model output were averaged over 5° L_s and 4° latitude bins. Model output was removed where no data was available. TES observed absorption optical depths were approximately scaled to extinction optical depths in the visible using the relation given in Smith (2004).
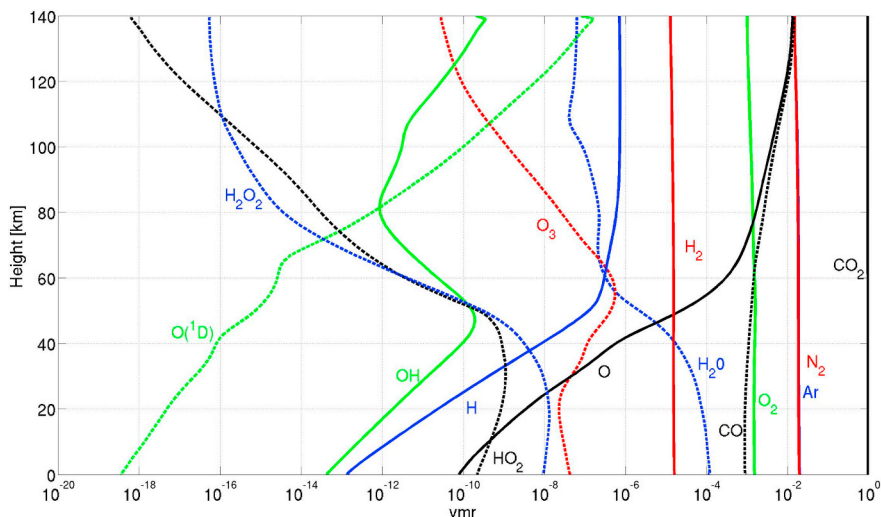
Fig. 5. Global and annual mean vmr profiles of the species included in the model.
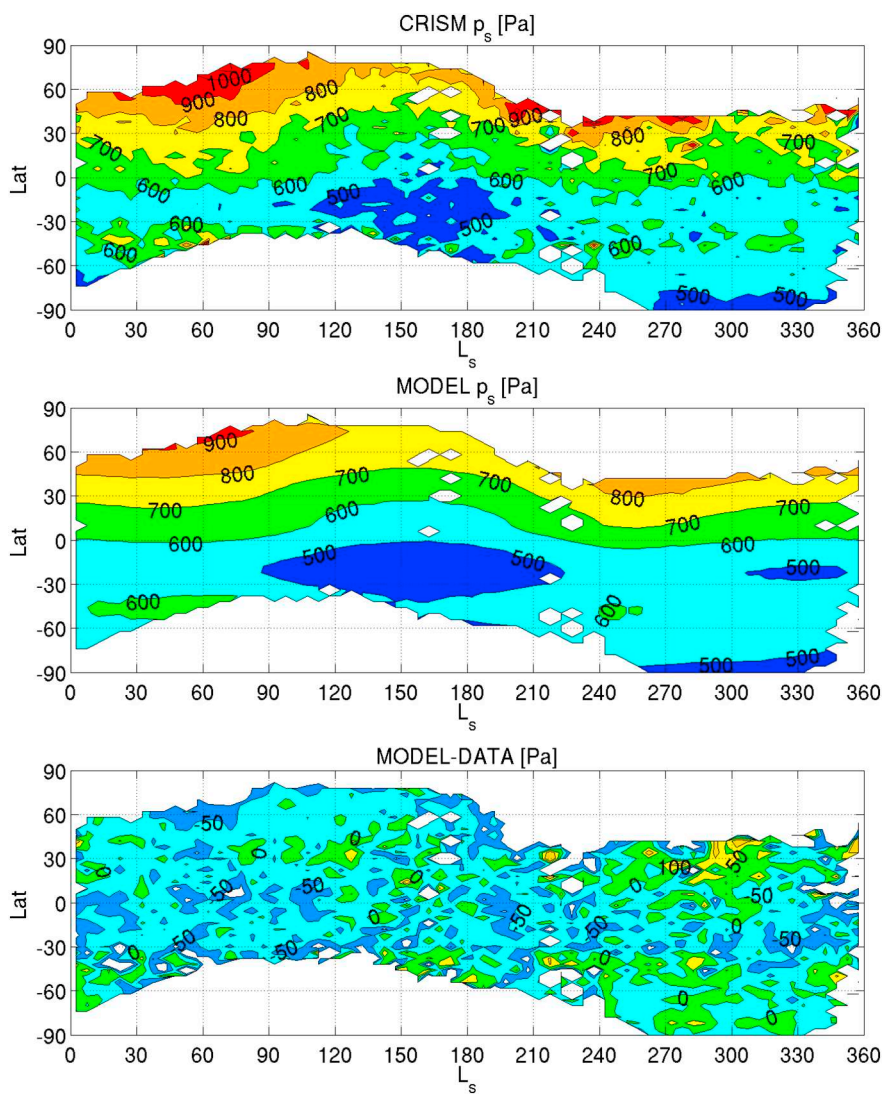

Fig. 6. Seasonal and latitudinal variation of the surface pressure observed by CRISM (Mars years 29–33, top) and simulated in the model (middle), and their difference (bottom). The model results are for daytime conditions (2–4 p.m., SZA < 80°). Data and model output were averaged over 5° L_s and 4° latitude bins. Model output was removed where no data was available.
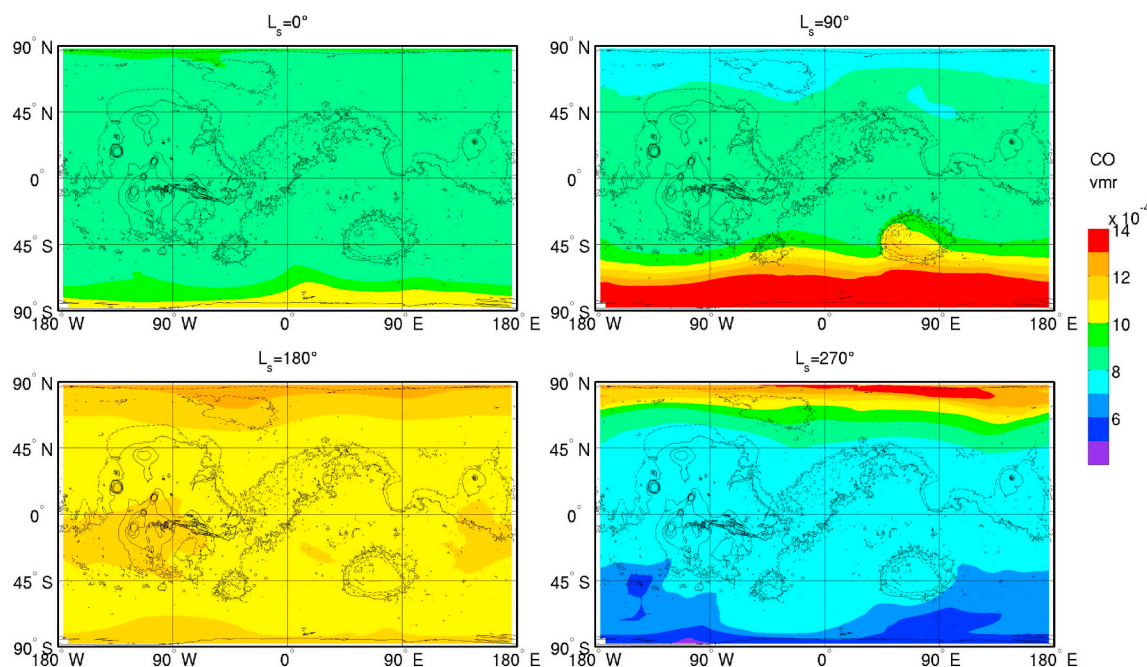
Fig. 7. Seasonal and latitudinal variation of CO column-integrated mixing ratio observed by CRISM (Mars years 29–33, top) and simulated in the model (middle), and their difference (bottom). The model results are for daytime conditions (2–4 p.m., SZA < 80°). Data and model output were averaged over 10° L$_s$ and 10° latitude bins. Model output was removed where no data was available.

versions available to the community, under the GNU Lesser General Public Licence v2.1. Many physical parameterizations were added, improved or extended, and thoroughly validated (Daerden et al., 2015; Viscardy et al., 2016; Neary and Daerden, 2018; Smith et al., 2018; Musiolik et al., 2018).

The present paper provides in detail observational evaluation of the atmospheric chemistry simulations and as such complements the work published on the LMD model chemistry simulations. The GEM-Mars model has a different formulation and dynamical core, and is code-wise fully independent of the LMD model. Among the main differences are the semi-Lagrangian semi-implicit transport scheme, and a very high vertical resolution. Thus for the first time, a view is presented on the Martian atmospheric chemistry from a different perspective, which provides a platform for inter-model comparisons that will foreseeably lead to improved understanding of the chemistry on Mars.

2. Model description

2.1. General model description

GEM-Mars is a General Circulation Model for the atmosphere of Mars with online atmospheric chemistry. The model is operated on a grid with a horizontal resolution of 4° × 4° and with 103 vertical levels

reaching from the surface to ~150 km. It calculates atmospheric heating and cooling rates by solar and IR radiation through atmospheric CO_2 and dust and ice particles, and solves the primitive equations of atmospheric dynamics. The code is fully parallelized using OMP and MPI and is typically run on 18 or 24 nodes. The geophysical boundary conditions (topography, albedo, thermal inertia and roughness length) are taken from observations (Neary and Daerden, 2018). Physical parameterizations in the model include an interactive CO_2 condensation/surface pressure cycle, a fully interactive water cycle including cloud radiative feedbacks, a thermal soil model including subsurface ice, interactive dust lifting schemes for saltation and dust devils, turbulent transport in the atmospheric surface layer and convective transport in the planetary boundary layer (PBL), subgrid scale vertical mixing in the free troposphere, a low level blocking scheme dealing with sub-grid scale topography, gravity wave drag, molecular diffusion, non-condensable gas enrichment, and atmospheric chemistry. A detailed description of the model, its formulation, grid, dynamical core and physical parameterizations, together with extensive validation against multiple datasets, was given in Neary and Daerden (2018).

The implementation of active dust lifting was described and evaluated in Daerden et al. (2015). Recently the model implemented the new threshold for saltation that was measured under Mars gravity conditions, and as such provided evidence that the new, experimentally

Fig. 8. Horizontal distribution of the CO column-integrated mixing ratio at the four cardinal seasons. The maps are instantaneous (so local time varies with longitude), non-averaged snapshots. The local true solar time is noon at 0° longitude in all maps.

found threshold allowed for the simulation of the dust cycle in a Mars GCM (Musiolik et al., 2018). The model simulates a general dust cycle with a low dust aphelion season and a dusty perihelion season. The freely simulated dust cycle shows some deviations from observations in the dusty perihelion season, a problem seen in many GCMs (e.g., Kahre et al., 2006).

Another application of the model is a study of the vertical distribution of methane shortly after a surface emission (Viscardy et al., 2016). As methane is expected to be present in the atmosphere at most at very low abundances, such emissions were found to lead to important variability on short time scales (weeks) as they distort the low atmospheric background. GEM-Mars output was also provided as a priori information for retrieval algorithms that are developed for the NOMAD instrument on ExoMars TGO (Vandaele et al., 2015; Robert et al., 2016, 2017; Vandaele et al., 2018). Most recently, the simulations of water vapor and CO in GEM-Mars were evaluated using the latest multi-annual retrievals by the Compact Reconnaissance Imaging Spectrometer for Mars (CRISM) on MRO (Smith et al., 2018). These results showed a global consistency with the data. The water cycle is, despite its simple formulation (see below) comparable to that simulated in more complicated models (e.g. Navarro et al., 2014a, 2014b). The simulation of the seasonal cycle of the CO column is also similar to that of non-condensables in other GCMs (Lefèvre and Forget, 2009; Lian et al., 2012).

The model can contain as many tracers as possible within the memory constraints of the computing machine. With the semi-Lagrangian, semi-implicit advection scheme, the number of tracers has no strong impact on computation time. A recent test included 120 tracers. The current basic setting consists of 6 tracers for dust (containing two 3-size bin distributions for dust lifted by saltation and in dust devils), 16 tracers for chemical composition (CO_2, Ar, N_2, O_2, CO, H_2O, CH_4, O_3, $O(^1D)$, O, H, H_2, OH, HO_2, H_2O_2 and $O_2(a^1\Delta_g)$), and 1 for water ice.

The water cycle in the model is currently very simple. Water condenses at saturation (100% relative humidity (RH)), or at any other imposed level of supersaturation (RH > 100%), and is stored in the water ice tracer, from which it can sublimate if conditions fall below saturation. The water ice tracer is actively applied in 2 processes: (i)

sedimentation and (ii) radiative feedbacks. In both processes a fixed water ice particle radius of 4 µm is assumed, except in the sedimentation below 10 km, where a radius of 8 µm is assumed. There is no direct interaction between the water and the dust. This leads to a reasonable simulation of the seasonal evolution of the water vapor vertical column compared to the observations, as will be shown below. See Neary and Daerden (2018) and Smith et al. (2018) for more details.

2.2. Atmospheric chemistry

The GEM-Mars model has fully interactive photochemistry (15 reactions) and gas-phase chemistry (31 reactions), taken from García Muñoz et al. (2005). The reactions are listed in Tables 1 and 2.

A difference with Lefèvre et al. (2004) is that $O_2(a^1\Delta_g)$ is explicitly considered as a species in the GEM-Mars model. The destruction of $O_2(a^1\Delta_g)$ is controlled by radiative relaxation (J15) and by quenching (R30). The effective lifetime of $O_2(a^1\Delta_g)$ is dominated by the fastest of these reactions, and is longer than the model timestep for altitudes above ~5–10 km, which justifies the explicit treatment of this excited state. The reaction rate of the relaxation (J15) is constant, but in the model it is attenuated along the line-of-sight by dust as for the other photolysis reactions, to simulate the airglow as it is observed from orbit, and then its behavior is numerically almost coinciding with J10.

All rates are taken from García Muñoz et al. (2005), except R30 which was reduced. Clancy et al. (2017) suggested a reduction to 0.25×10^{-20} cm^3 s^{-1}, which is now applied in the model. In three body reactions, the efficiency is greater when the third body is CO_2 compared to other molecules. When no rate coefficient is available for CO_2, the ratios of rate coefficients for different species were taken from Lindner (1988). E.g. for R24, the rate in N_2 is $6 \times 10^{-34} \times (T/300)^{-2.4}$ (Burkholder et al., 2015). Following Lindner (1988), the rate in CO_2 is then a factor 2.3 higher, resulting in the value reported in Table 2.

The actinic solar flux is the same one as in García Muñoz et al. (2005) except that it is (for computational efficiency) coarse-grained from the original 247 wavelength bins grid to a 47 bin wavelength grid, ranging from 5 to 250 nm. The solar flux is scaled following the exact position of Mars in its orbit and its distance to the sun, following the expressions of Allison (1997) and Allison and McEwen (2000). The
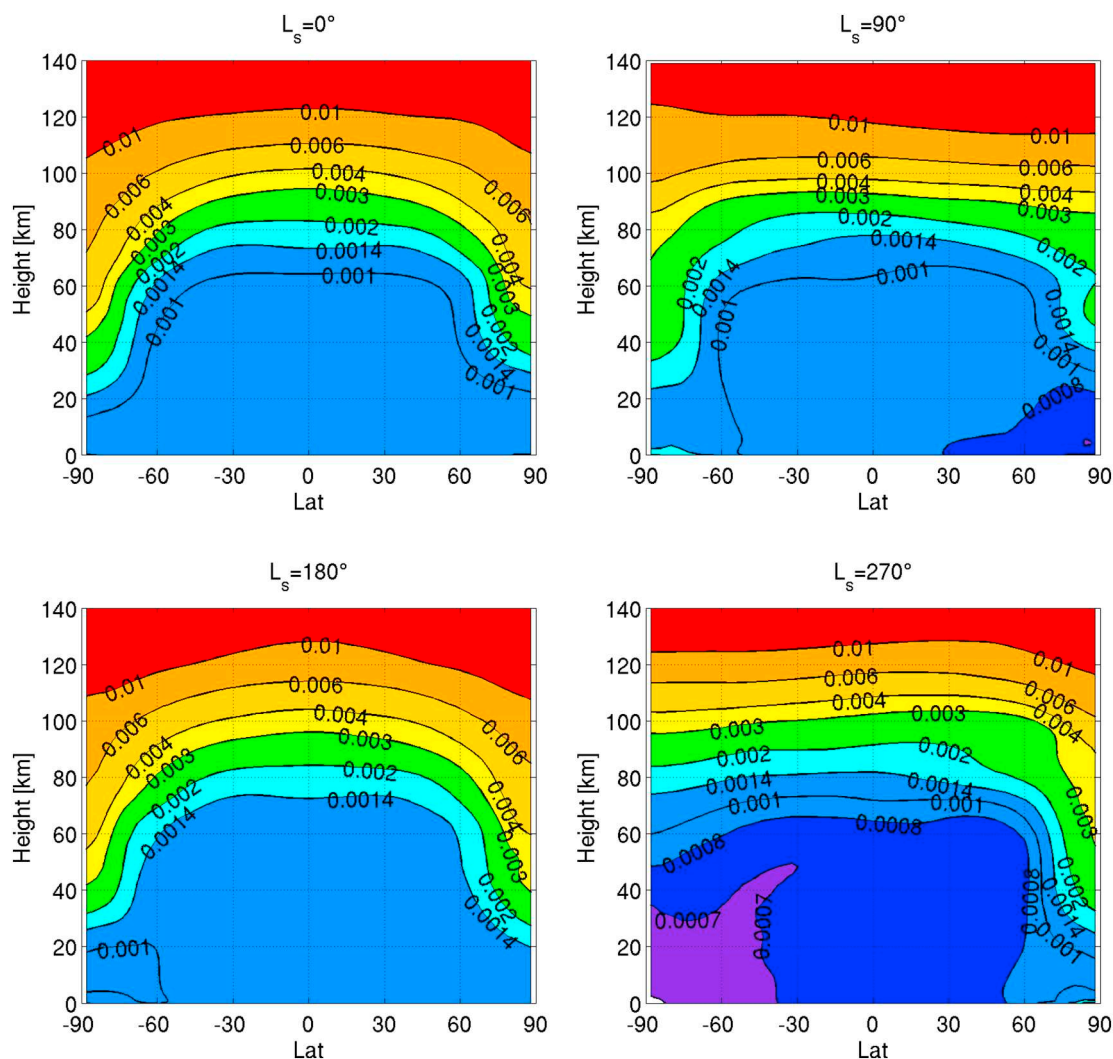
Fig. 9. Latitude-height zonal mean vertical distribution of the CO vmr (logarithmic color scale) for the four cardinal seasons. The vmr was averaged over all longitudes (and local times) and over 10 sols.

absorption cross-sections and quantum yields are taken as in García Muñoz et al. (2005) and coarse-grained to the same 47 bin wavelength grid. The photolysis and reaction rates are calculated online in the model. The optical path is calculated using the method of Brasseur and Solomon (2005, Box 4.1), assuming spherical symmetry. For the transmissivity, absorptions by CO_2, O_2, O_3, H_2O, HO_2 and H_2O_2, as well as attenuation by dust and water ice, along the line of sight are taken into account. Rayleigh scattering is not taken into account. Mars Rayleigh opacities are small compared to aerosol extinction (Ityaksov et al., 2008). It was verified (not shown) that Rayleigh scattering will affect some results (such as for O_3 and H_2O_2) by at most ~10% depending on season and latitude, which is comparable to other uncertainties in the model.

Special attention was paid to the absorption cross-sections of CO_2 and the photolysis of water (J11). For CO_2, at wavelengths longward of 165.5 nm, we used the cross-sections reported by Parkinson et al. (2003) for two temperatures. Measurements are available up to 192.5 nm at 195 K and up to 200 nm at 295 K. At those wavelengths, the cross-sections are still far from being negligible. Following the assumptions made by Lefèvre et al. (2004), the cross-sections were derived by linear extrapolation of the logarithm of the measured data up to 210 nm. This extrapolation matches very well with recent measurements at low temperatures (Venot et al., 2018). The photolysis of water vapor (J11) in the lower atmosphere of Mars is known to be very sensitive to the H_2O absorption cross-sections at wavelengths longward

of 180 nm (Lefèvre et al., 2004). To the best of our knowledge, the cross-sections reported by Chung et al. (2001) on a fine wavelength grid (0.2 nm) at 250 K are the most appropriate data for photochemical models of the Martian atmosphere (F. Lefèvre, private communication). We thus used these measurements, which were linearly extrapolated with the logarithm of the cross-sections up to 196 nm.

The photolysis rates for all reactions are plotted in Fig. 1 under the following conditions: local noon at northern hemispheric solstice, at 40°N, 0°E. The model state for this time and location was: solar zenith angle (SZA) = 15°, visible dust optical depth of ~0.3, surface pressure ~780 Pa, and a total O_3 column of ~1.4 μm-atm. The rates of the 2- and 3-body reactions for the same conditions are shown in Fig. 2. Fig. 3 shows the simulated vertical profiles of the vmr of the species at the same place and time.

Nitrogen chemistry is currently not included in the model. This has a small but non-negligible impact on the simulations, as the reaction of NO with HO_2 is an indirect source of O_x and increases the ratio OH/HO_2 in the lowermost atmosphere (Krasnopolsky, 1993; Lefèvre et al., 2004; Lefèvre and Krasnopolsky, 2017), and also because catalytic cycles involving NO_x are expected to contribute for 5–10% in the production of CO_2 (Lefèvre and Krasnopolsky, 2017). Nitrogen chemistry will be implemented in a future version of the model.

Three species can undergo phase changes: CO_2, H_2O and H_2O_2. CO_2 condensation/sublimation is taken into account following a method similar to Forget et al. (1998), see Neary and Daerden (2018). This
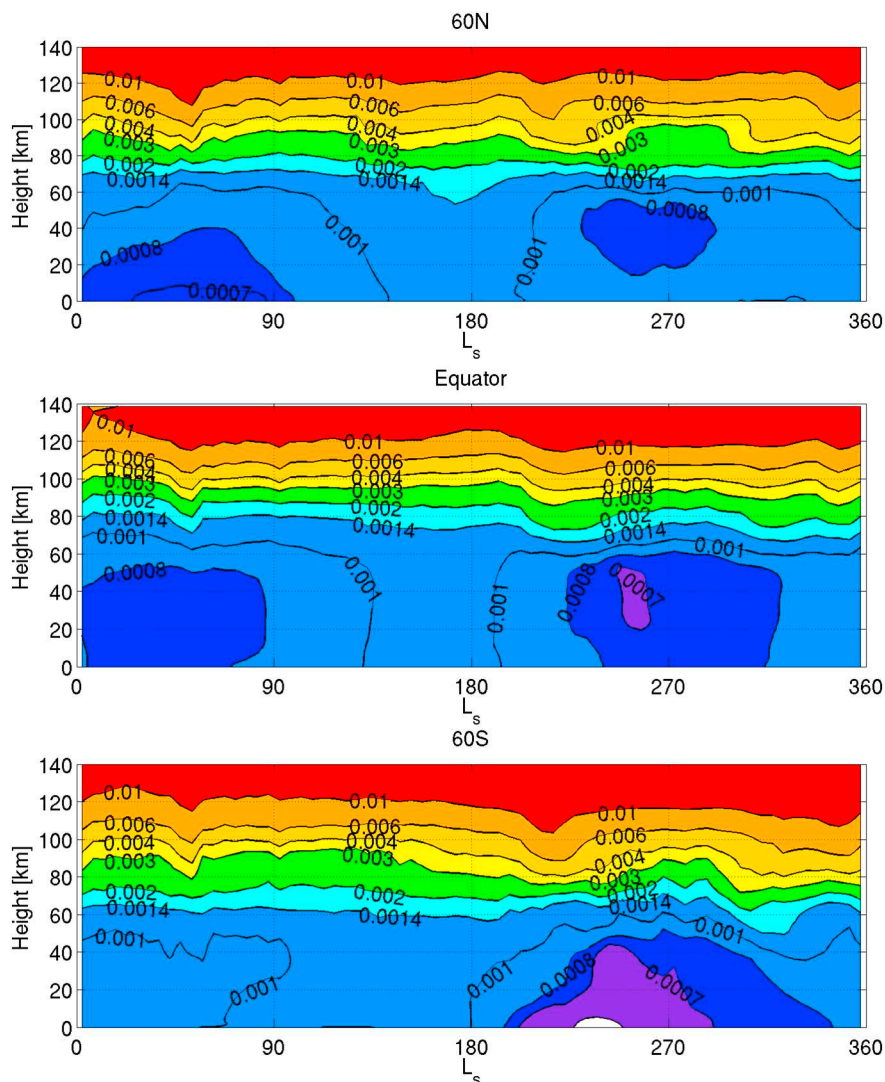
Fig. 10. Seasonal variation of the zonal mean CO vmr vertical profile at 3 latitudes. The vmr was averaged over all longitudes and local times in 5° L_s bins.

method uses the atmospheric state variables as input and calculates the impact on the surface pressure, and does not change the vmr of CO_2 in the model. To implement the changes in the vmr of all species upon condensation/sublimation of CO_2, a simple parameterization was developed (Smith et al., 2018), in which the vmr of CO_2 is updated with a factor proportional to the ratio of the number density of CO_2 in newly formed ice to the air number density (or using the total column in the case of sublimation from the surface). The vmr of the other species is then updated in order to keep their sum equal to unity. The resulting simulations of polar enhancement of Ar and CO vmrs are in reasonable agreement with observations (Neary and Daerden, 2018; Smith et al., 2018). The mass of air is updated in the model according to the actual composition, which means that it becomes variable and can deviate from the average value of 43.34 g/mol. The updated air mass is applied in most physics routines, but not in the dynamical core where it is technically more complicated to modify, and where the average value is applied (this is envisaged to be modified in the future).

The formation of water ice has been described above, see Neary and Daerden (2018) and Smith et al. (2018) for more details. Finally, H_2O_2 is permanently removed from the model if it becomes saturated following the expression given in Lindner (1988). (While this is an approximation, the impact on H_2O_2 loss in the model seems negligible, but this will be improved in future model versions.)

No escape fluxes are defined at the top of the model. The vmr of H_2 is kept at 15 ppm by volume (ppmv) at all times and places (Krasnopolsky and Feldman, 2001), which is justified by its long lifetime of 300 years in the lower atmosphere (Lefèvre and Krasnopolsky, 2017).

To avoid complications related to atmospheric stability over long timescales (i.e. photolysis of CO_2 and recycling of O_2 and CO into CO_2 by the interaction of water vapor photolysis products, and neglecting the nitrogen chemistry cycle), the vmr of CO_2, O_2 and CO are not updated below 20 km after the chemistry module is executed. When this is not done, there is a small drift in the abundances of CO and O_2. On the timescale of our simulations (a few Mars years) this effect is very small.

3. Simulations

3.1. Model constraints and initialization

The objective of this paper is to present the chemistry simulations in the current state of the model as presented in Neary and Daerden (2018) and Smith et al. (2018). The atmospheric chemistry depends principally on the dynamics, that is controlled by atmospheric dust and water ice clouds, and on the distribution of water vapor. To allow for a meaningful evaluation of the chemistry simulations, the model has to include reasonably good dust and water cycles. While the current implementation of these cycles is simple, we are convinced that they
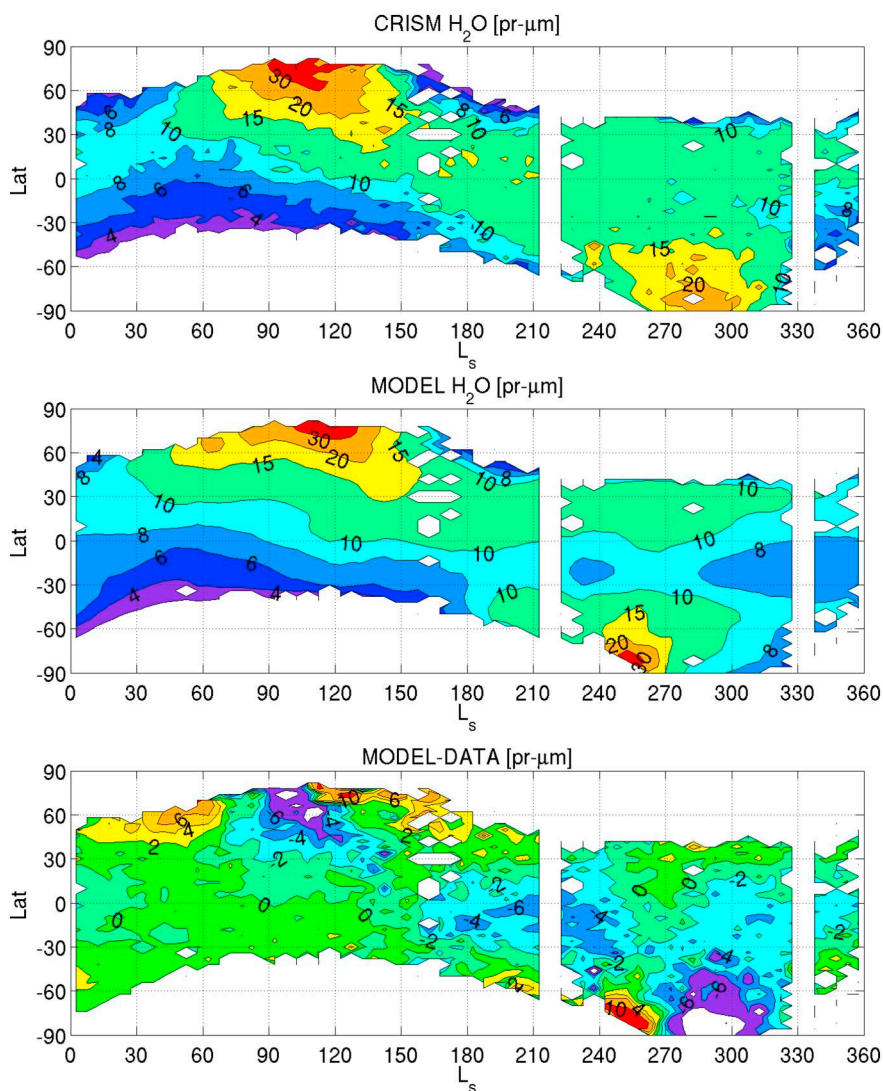
Fig. 11. Seasonal and latitudinal variation of the total vertical column abundance of H_2O observed by CRISM (Mars years 29–33, top) and simulated in the model (middle), and their difference (bottom). The model results are for daytime conditions (2–4 p.m., SZA < 80°). Data and model output were averaged over 5° L_s and 4° latitude bins. Model output was removed where no data was available.

incorporate sufficiently well the main features that are known from observations. The Mars dust cycle is simulated actively and freely in the model and is not constrained by any dust optical depth observations. The dust lifting efficiency factor is set such that the simulated dust cycle resembles an average non-dust storm year. The simulated dust cycle is compared to observations from TES (Smith, 2004) in Mars year 26 in Fig. 4. The general pattern of a low dust and high dust season is re-produced, and the optical depths are of the right order of magnitude. At present the model is unable to simulate two dust peaks that are typi-cally observed in the dusty season, and simulates rather one broad peak. We don't expect this to have a big impact for the atmospheric chemistry results presented in this paper. In reality these dust peaks are variable from year to year (Montabone et al., 2015), while O_3 column observations were found to show no significant inter-annual variability (Clancy et al., 2016), O_2 airglow observations showed little inter-annual variability (Guslyakova et al., 2016), and water vapor observations only showed significant changes during major dust storms (Trokhimovskiy et al., 2015; Fedorova et al., 2018; Smith et al., 2018). Therefore, we do not include simulations with different dust settings. In the comparisons to data, we will leave out observations of Mars year 28, when a global dust storm occurred.

The model was initialized by the final atmospheric state at $L_s = 0°$ of

the multi-annual simulation presented in Neary and Daerden (2018), except for the chemistry tracers apart from water vapor. CO_2, Ar, N_2 and O_2 were initialized by the values reported in Mahaffy et al. (2013). CO was initialized uniformly to 800 ppmv (Smith et al., 2018), and H_2 to 15 ppmv (Krasnopolsky and Feldman, 2001). The other tracers were initialized to zero. The model results presented here were taken from the second Mars year of the simulation. It was verified that interannual variability for the later years is negligible. The orbital settings (Mean Solar Time on the Mars prime meridian at the start of the year) for this second year of simulation are for Mars year 28. The simulated annual mean profiles of all species are shown in Fig. 5. Below results will be presented in more detail for the main species for which observations are available: CO, H_2O, H_2O_2 and O_3, and $O_2(a^1\Delta_g)$ airglow, with focus on daytime conditions. Where we find biases between the simulated chemistry tracers and the observations, these will be discussed in terms of the dust and water simulations.

3.2. Carbon dioxide

Carbon dioxide (CO_2) is the principal constituent of the Martian atmosphere. It is photolyzed mainly by J2 (see Table 1 and Fig. 1) with a photochemical lifetime of ~3000 years. It was found that this reaction
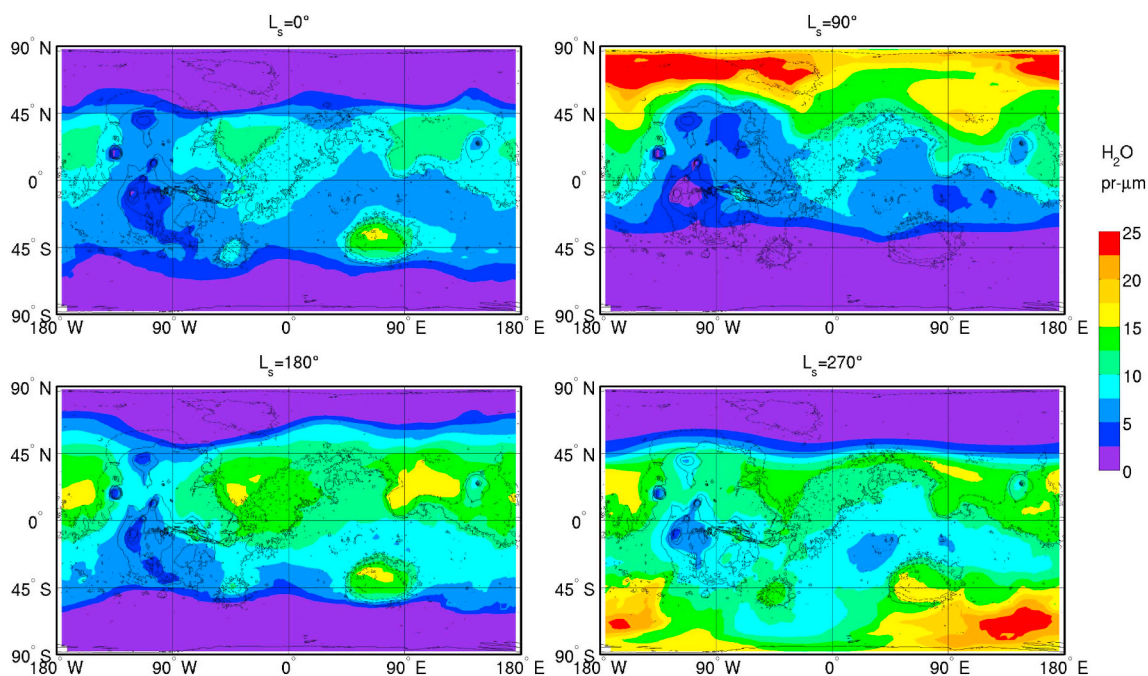
Fig. 12. Horizontal distribution of the total vertical column abundance of H_2O (in pr-μm) at the four cardinal seasons. See Fig. 8 for more details.
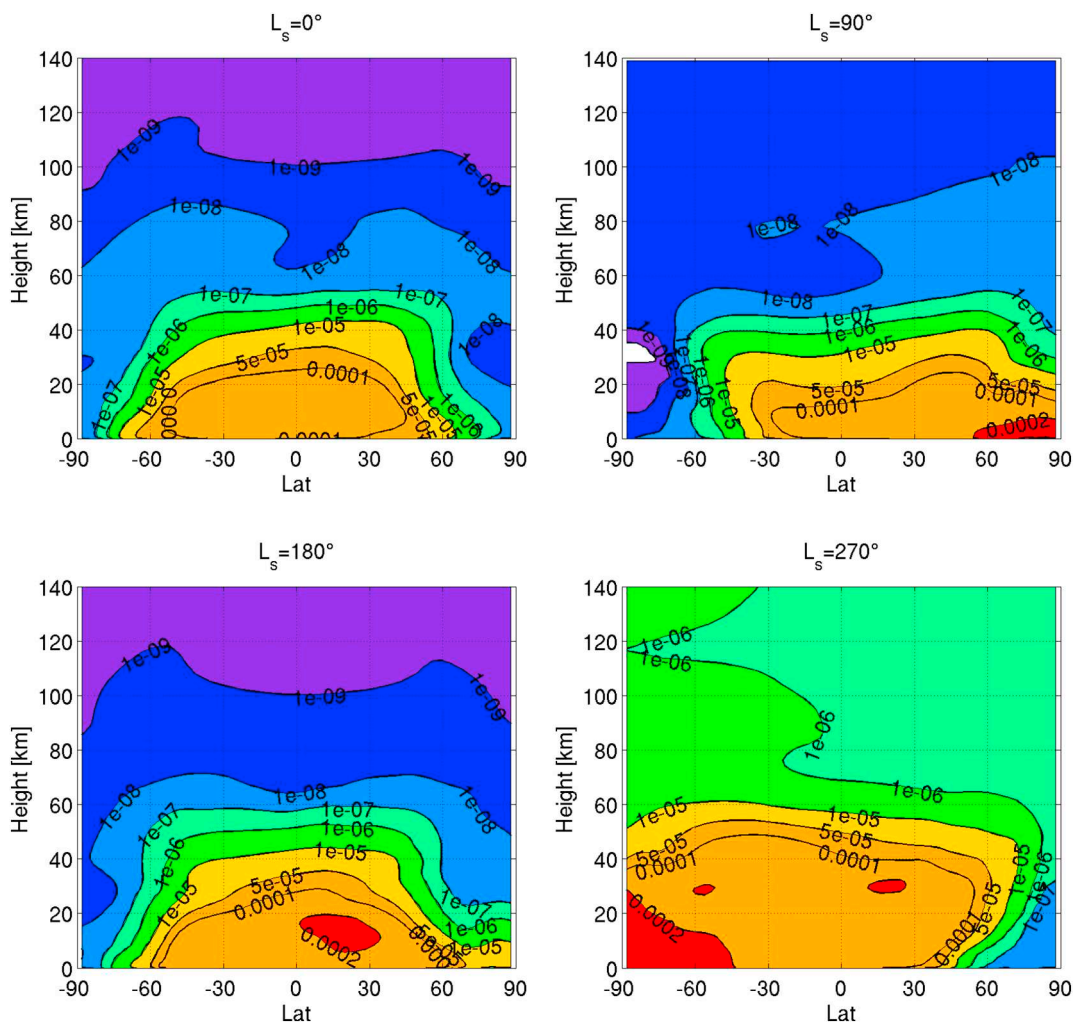

Fig. 13. Latitude-height zonal mean vertical distribution of the H_2O vmr for the four cardinal seasons. The vmr was averaged over all longitudes and local times and over 10 sols.
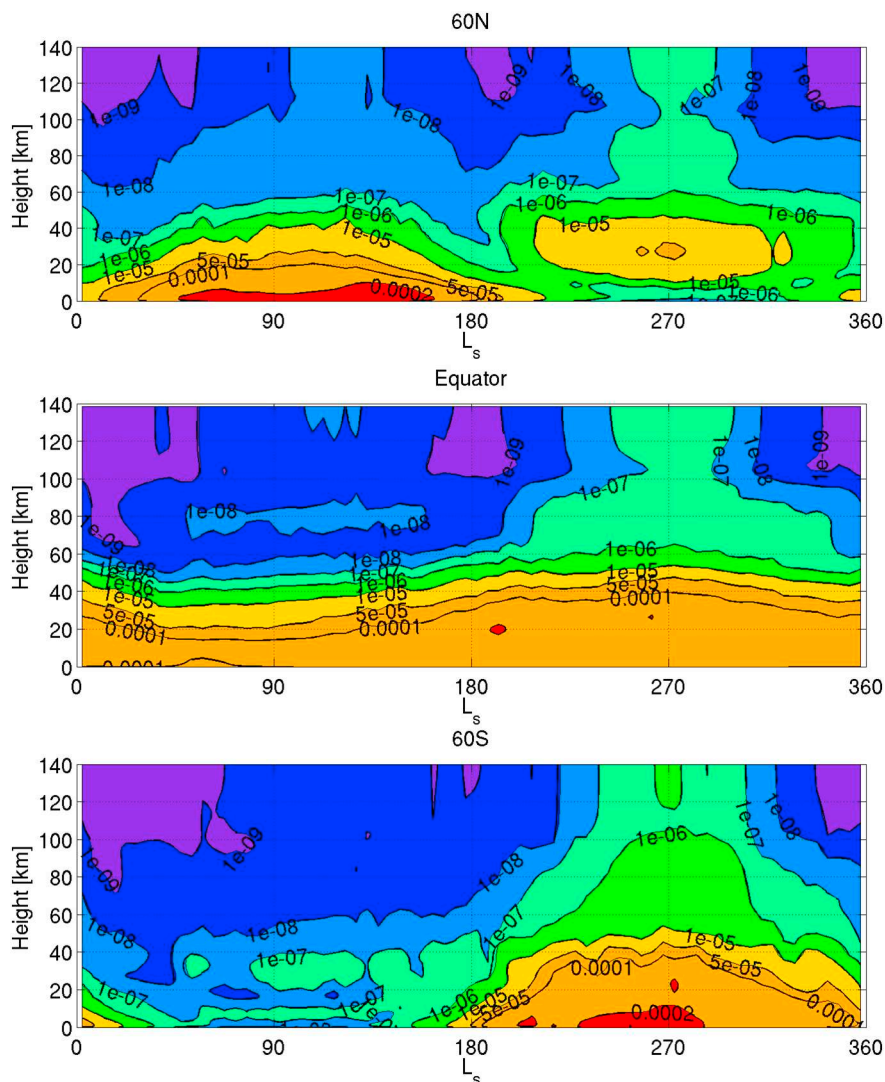
Fig. 14. Seasonal variation of the zonal mean H_2O vmr vertical profile at 3 latitudes. The vmr was averaged over all longitudes and local times in 5° L_s bins.

is counteracted by reactions involving photolysis products of water vapor, mainly through R1 (Table 2), so that water vapor helps to stabilize the Martian atmosphere (McElroy and Donahue, 1972; Parkinson and Hunten, 1972; Lefèvre and Krasnopolsky, 2017). Such long-term processes are beyond the scope of this paper, in which we focus on seasonal scale chemistry. On such scales, the condensation/sublimation cycle of CO_2 is far more important. This was already explained in detail above (Section 2) and in previous publications (Neary and Daerden, 2018; Smith et al., 2018).

Observations of column-integrated CO_2 allow to derive surface pressure, and so surface pressure provides a direct indication of the total column abundance of CO_2. A direct comparison of surface pressure as derived from observations by CRISM with the model simulations was presented in Smith et al. (2018). For completeness we include the comparison here again in Fig. 6. The match with the data is overall very good, both for absolute values as for the seasonal and latitudinal variability. Such a good correspondence is an important requisite for a good simulation of the atmospheric chemistry.

3.3. Carbon monoxide

Carbon monoxide (CO) is a relatively long-lived species with only weak variability due to chemistry. It does not condense with CO_2 and its relative abundance is controlled by the effects of the CO_2 condensation,

which leads to a distinctive seasonal pattern (Smith et al., 2018). Still it plays an important role in Mars atmospheric chemistry, and it is important to present how it behaves in the model. The seasonal cycle of the vertically integrated column of CO (relative to CO_2, so column-averaged vmr) observed by CRISM and the corresponding simulation are shown in Fig. 7. This simulation was discussed in detail in Smith et al. (2018). We here repeat the main features. The CO_2 condensation/sublimation cycle causes distinct seasonal and latitudinal trends in the CO column, with an increase at all latitudes in the middle of the year, and a decrease at polar latitudes during local spring and summer. The polar depletion is stronger in the south. In the simulation, the mid-year column increase does not last as long as in the data, where it seems to continue throughout a large part of the dust season. Also the polar depletion does not last as long in the simulation as in the data. This may highlight shortcomings in terms of circulation patterns and mixing processes in the GCM. See Smith et al. (2018) for more discussion.

Maps of the simulated CO column-averaged density are shown in Fig. 8 for the four cardinal seasons. The simulated vertical distribution of CO for the four cardinal seasons is shown in Fig. 9. The impact of the CO_2 condensation/sublimation cycle is mainly visible in the polar regions. At present there is no observational information about the vertical distribution of CO to compare with (CO vmr profiles will be among the main science returns of the TGO mission, Vandaele et al. (2015, 2018)). The result for $L_s = 90°$ can be compared to Fig. 3 in the

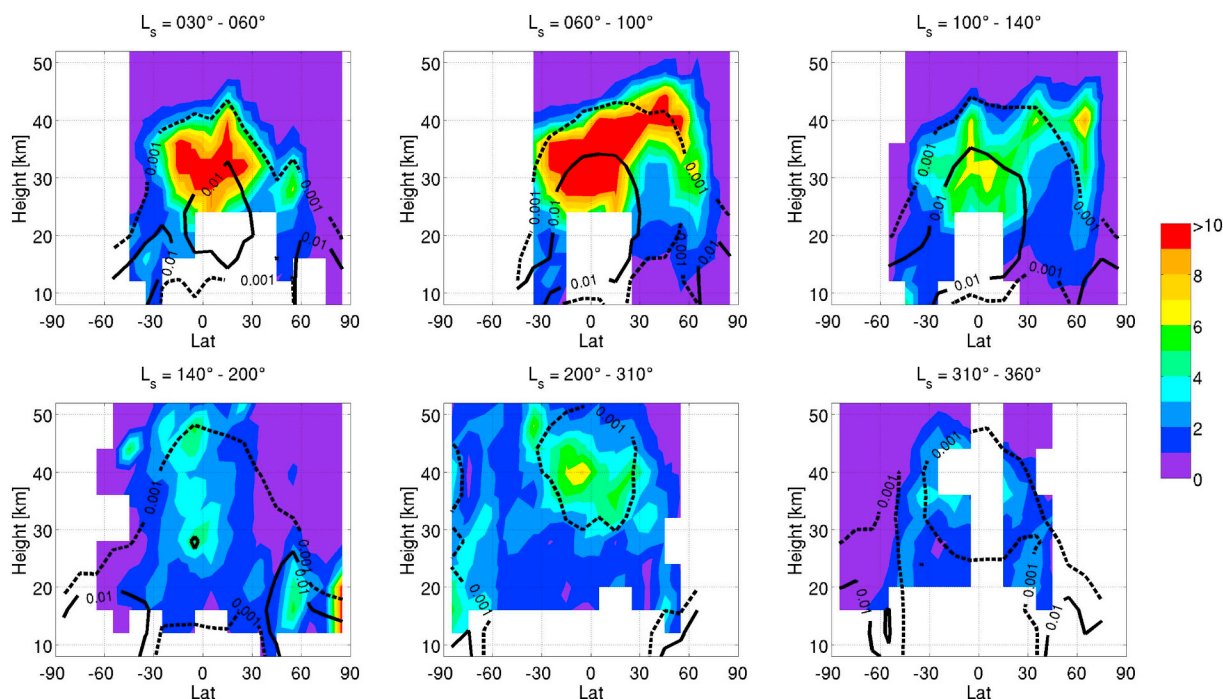**Fig. 15.** Latitude-height distribution of the ratio of H_2O vmr in GEM-Mars over CRISM "derived H_2O" for 6 L_s periods throughout the year. GEM-Mars profiles were first interpolated to the CRISM time, location and altitude grid. The added black contours are for GEM-Mars water ice cloud extinction of $10^{-2}\,km^{-1}$ (full) and $10^{-3}\,km^{-1}$ (dashed).
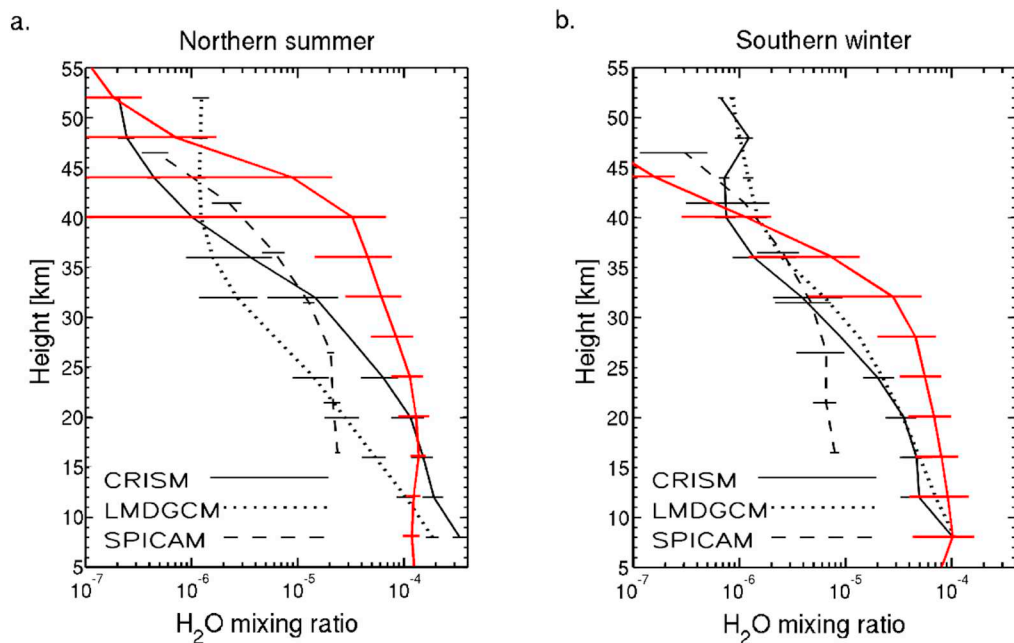

Fig. 16. Averaged water vapor profiles for (a) $L_s = 80°$-$105°$, latitude = 40°N-60°N and (b) $L_s = 90°$-$110°$, latitude = 40°S-20°S. Figure reproduced from Clancy et al. (2017), Fig. 15, with CRISM and co-located LMD GCM averaged profiles, and SPICAM direct water vapor observations in the same range but not co-located. Red lines are GEM-Mars simulated water vapor profiles, co-located to the CRISM profiles, and their 1 sigma variability. (For interpretation of the references to color in this figure legend, the reader is referred to the web version of this article.)

Supplementary Information of Lefèvre et al. (2008), the correspondence is good. Fig. 10 finally shows the seasonal evolution of the zonal mean CO vmr at the equator and at 60°N/S latitude. The increase of the vmr below ~60 km starts in the south around $L_s \sim 90°$, reaches the equator around $L_s \sim 120°$ and reaches high northern latitudes by $L_s \sim 150°$. An opposite but much weaker enhancement is starting in the north around $L_s \sim 300°$ and reaches the southern latitudes by $L_s \sim 330°$.

3.4. Water vapor

Simulation results for water vapor total columns were presented and discussed in Neary and Daerden (2018) and Smith et al. (2018). For completeness we include here the comparison of the simulated water vapor column to retrievals from CRISM in Fig. 11. The general seasonal and latitudinal trends are reasonably well simulated. The following regions of model-data bias can be identified:

1. Northern springtime and summer release of water vapor from the permanent cap and subpolar regions. The simulated values are of the right order but the problems are mainly in the timing of the releases. Among the causes for these biases are the model's coarse resolution compared to fine scale ice structures in the polar cap, the simplistic cloud scheme, and excessive cloud radiative feedbacks due to too thick polar hood clouds.
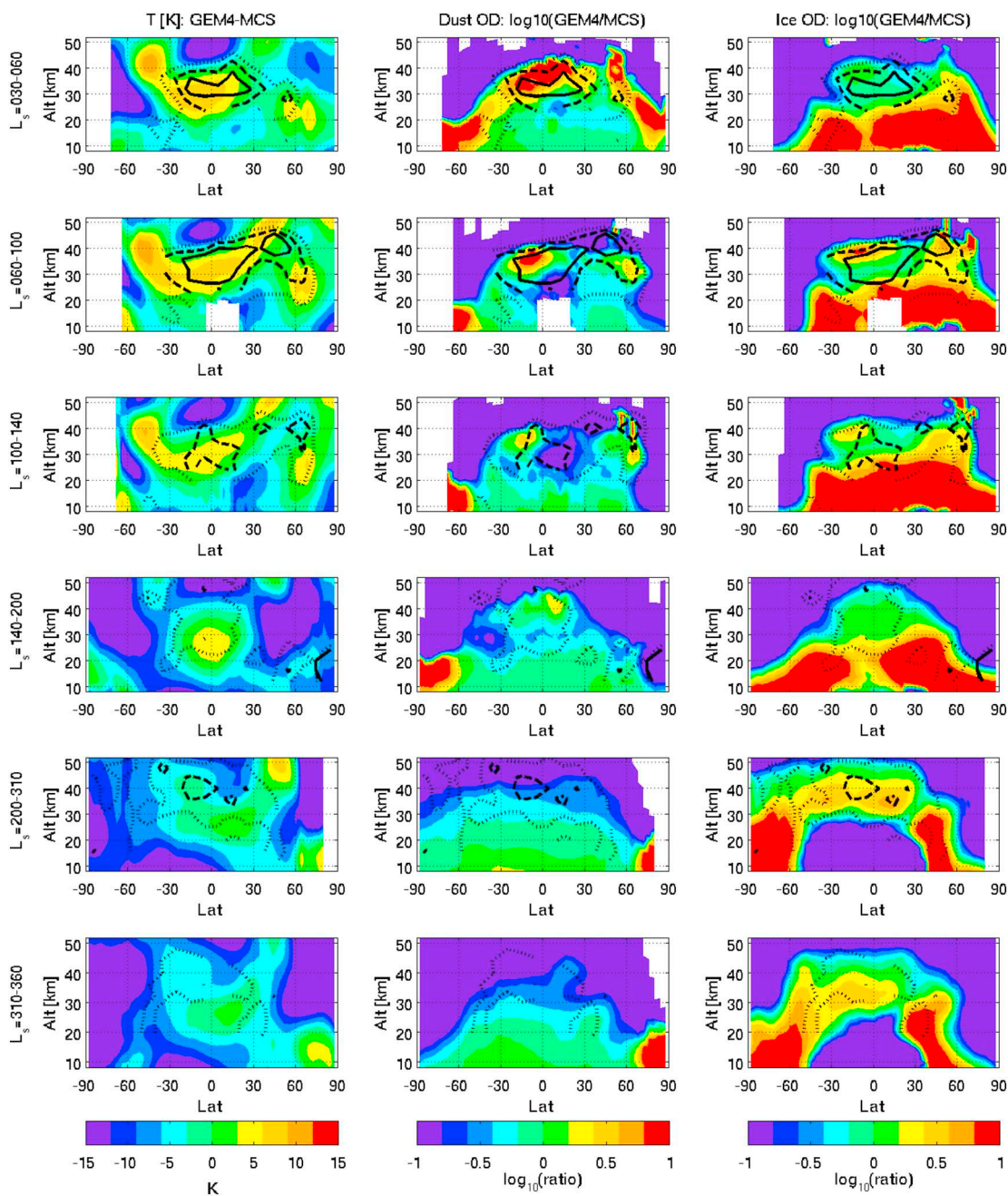
Fig. 17. Detailed comparison between GEM and MCS: temperature difference (left), and logarithm of the ratio of dust optical depth (center), and of ice optical depth (right). GEM-Mars output was interpolated to all daytime MCS V4 (2D retrieval) profiles of Mars year 31 within 1 h of the observation. The 6 L_s intervals (rows) correspond to the ones used for comparison to CRISM water vapor profiles in Fig. 15. The added contour lines are for the model/CRISM water vapor ratio of Fig. 15 for ratios of 10 (full), 5 (dashed) and 2 (dotted). MCS observed extinctions were approximately scaled to visible wavelengths using the relations given in Kleinböhl et al. (2011).

2. The south polar maximum which occurs more abrupt and less smooth in the model compared to the data. One of the issues that plays a role here is the simplistic prescription of the southern permanent CO_2 ice cap in the current model. In reality water vapor is residing in the south polar area (as vapor or in surface ice) for a longer time than is simulated in the model, and is released back into the atmosphere more gradually. As a result, the water distribution over the planet in the $L_s \sim 270°$–$330°$ season is too low in the simulations.

3. Between the equator and 30°S latitude in the $L_s \sim 180°$–$270°$ season the model water columns are lower than the observed ones. This may be related to meridional transport being too strong in the

model, which can also cause too much water to condense on the south polar cap (which also relates to the previous point).

Maps of the horizontal distribution of the water column are shown in Fig. 12 for the cardinal seasons. We refer to the already cited papers for more discussion.

Here we will discuss more in detail the vertical distribution of water vapor, because of its importance for the atmospheric chemistry. Fig. 13 shows the latitude-height distribution of water vapor at the four cardinal seasons, and Fig. 14 shows the seasonal evolution of the water vapor vmr at the equator and 60°N/S. As discussed in the introduction, vertical profiles of water vapor are one of the most unexplored
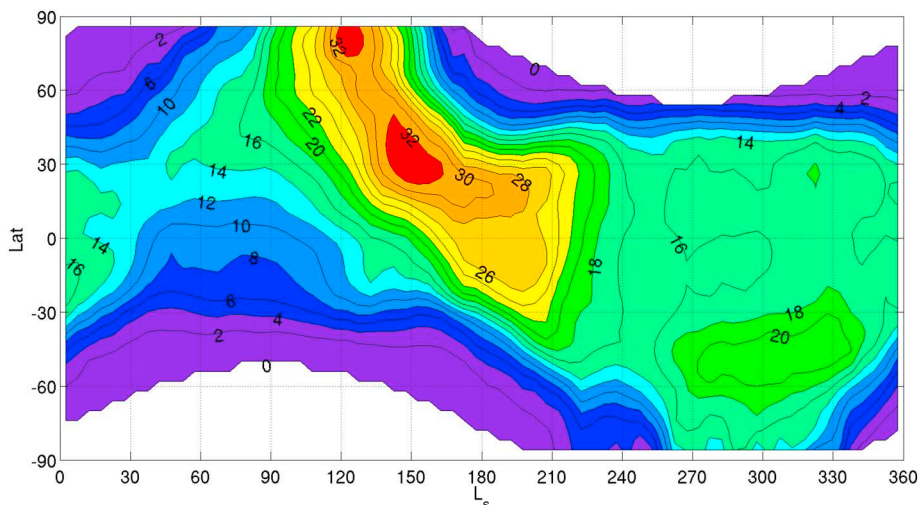
Fig. 18. Seasonal and latitudinal variation of the H_2O_2 column-integrated mixing ratio (in parts per billion, ppbv) simulated in the model for daytime conditions (SZA < 80°). Model output was averaged over 5° L_s bins.
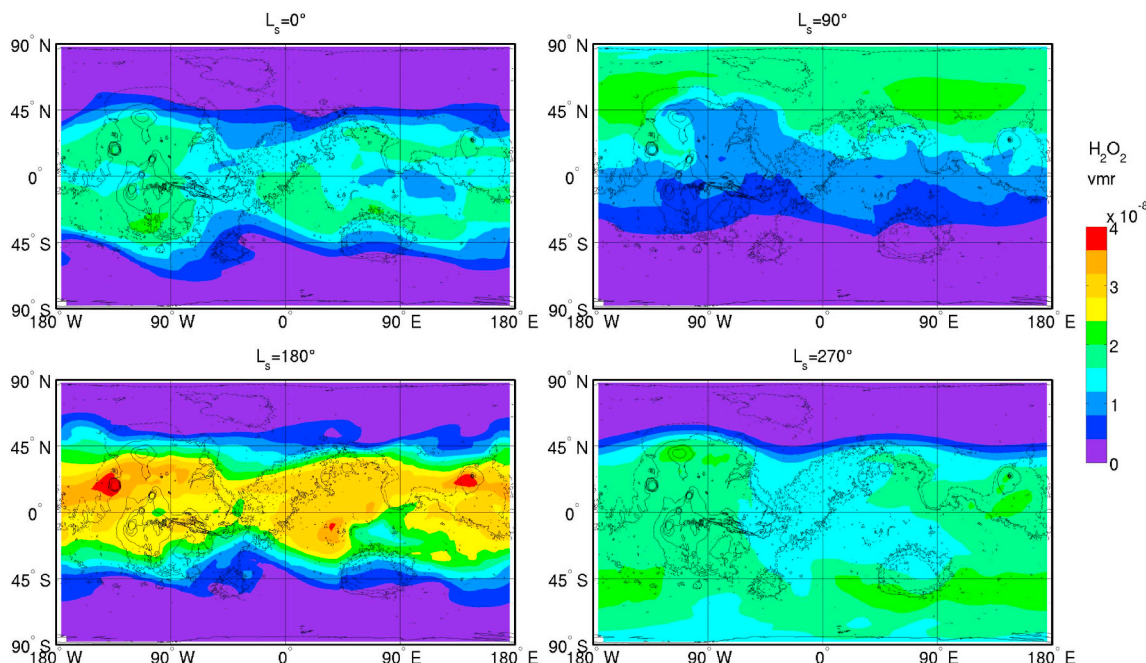
Fig. 19. Horizontal distribution of the total vertical column abundance of H_2O_2 at the four cardinal seasons. See Fig. 8 for more details.

quantities to date. Prior to the TGO mission, only two direct observations of the water vapor vertical profile are available, based on SPICAM solar occultation measurements: Maltagliati et al. (2011, 2013) and Fedorova et al. (2018). However, these datasets are sparse (about 100 profiles outside of dust storm conditions). One other study, Clancy et al. (2017), derived daytime vertical water profiles from CRISM oxygen airglow observations using model correlations, for lower altitudes (20–55 km) and with a denser seasonal coverage (few 100 profiles per season, ~1100 in total).

The GEM-Mars water vapor fields were interpolated to the time and location of the CRISM water vapor profiles, and then interpolated to the special grid used for the latter (see Clancy et al., 2017 for details). The maximum deviation in local time between the model state and the observation is 15 min. Fig. 15 shows the latitude-height distribution of the ratio of the water vapor vmr between GEM-Mars and CRISM, for 6 time periods defined in Clancy et al. (2017). The contours of the water ice cloud extinction simulated in GEM-Mars are added. Below typically 25 km, GEM-Mars water vapor does not differ from CRISM water vapor

by more than a factor 2. However, near the cloud top, GEM-Mars water vapor can be considerably higher than the CRISM water vapor, by factors 4 to > 10, with a strong seasonal dependency. The ratio is higher when the clouds are optically thicker (i.e. in the aphelion season).

Clancy et al. (2017), in their Fig. 15, provide a comparison of the CRISM derived water vapor profiles around aphelion to the contemporaneous SPICAM direct observations of water vapor at the terminator, and to the LMD model. Their figure is copied here in Fig. 16 with GEM-Mars simulated water vapor added. Both in the north and south, at 30–40 km altitude, CRISM and SPICAM water vapor abundances differ at most by a factor ~2–3, and GEM-Mars shows also a high bias with respect to SPICAM as it does for CRISM.

An explanation for this excess in water can be found when comparing the temperatures simulated in GEM-Mars to observations by the Mars Climate Sounder (MCS) instrument on MRO (McCleese et al., 2007). GEM-Mars temperature profiles were interpolated to all the daytime (SZA < 80°) MCS V4 (2D retrieval) profiles of temperature in
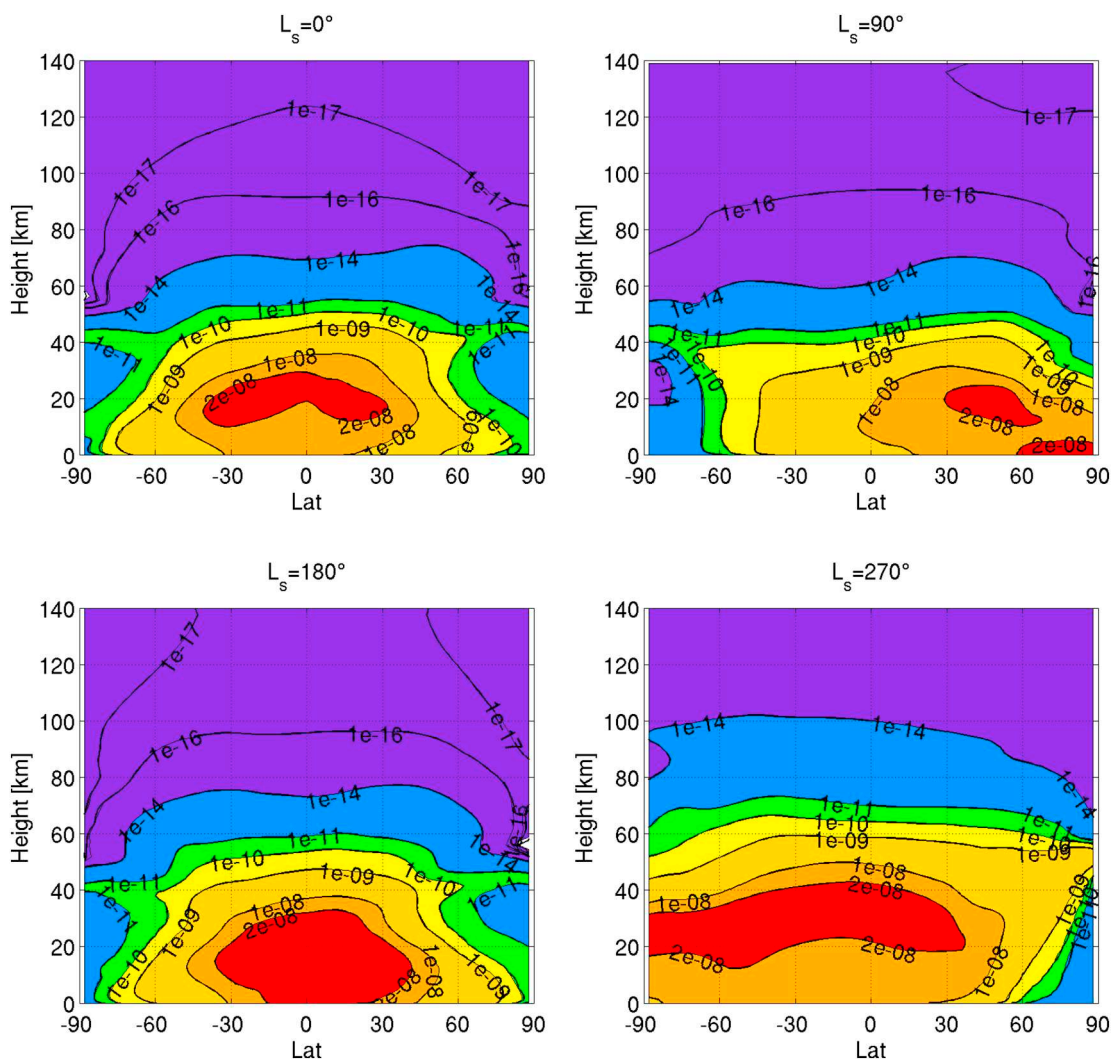
Fig. 20. Latitude-height zonal mean vertical distribution of the H_2O_2 vmr for the four cardinal seasons. The vmr was averaged over all longitudes and local times and over 10 sols.

Mars Year 31 (to within 1 h accuracy), and the data and model profiles were averaged over the same L_s-ranges as for the CRISM data. To allow using the model height as a vertical coordinate, the averaged MCS profiles (which have pressure as a vertical coordinate) were interpolated to the model pressure grid. The so obtained model-data comparison is shown in Fig. 17. Although the MCS profiles do not coincide with the CRISM profiles, the averages over the wide L_s intervals can be expected to be indicative of general trends that can provide insight into the model-CRISM water vapor biases (the typical number of MCS profiles in the shortest windows is ~10,000). When comparing Figs. 15 and 17, it has to be noted that they use a different altitude grid, but this involves differences of a few km at most. To facilitate the comparison, contour lines for the high water vapor ratios were added on Fig. 17 (without correcting for the altitude). This clearly indicates a correlation between the high positive water vapor biases and high positive temperature biases. Model temperatures are especially found to be very warm compared to MCS in and just above the aphelion cloud belt (ACB). Biases are much smaller outside of the ACB season. To understand the temperature biases, also a comparison of simulated to MCS dust and ice optical extinction is included in Fig. 17. This indicates that:

1. There is too much high altitude dust in the model before $L_s = 100°$, which is consistent with the model being too dusty at low latitudes compared to TES (see Fig. 2); and

2. The optical depths and resulting radiative warming of the clouds in the model are too strong between $L_s = 60°–140°$.

Both factors prevent water vapor to condensate sufficiently. While the problem for dust can be solved by constraining the simulated dust by observational climatologies, the way the water ice clouds are currently simulated in GEM-Mars is too simplistic, and more refined size distributions and microphysics are required, including dust-water ice interactions. We developed a detailed microphysical model for Mars ice clouds (Daerden et al., 2010), which is currently being implemented in the GEM-Mars model to address this. In addition, high vertical resolution water profiles with an unprecedented vertical coverage are expected from the TGO instruments NOMAD (Vandaele et al., 2018) and ACS (Korablev et al., 2018). These will significantly improve our knowledge about the vertical distribution of water vapor on Mars and provide important information to improve the water cycle in models.

3.5. Hydrogen peroxide

The photolysis products of water, OH and HO_2, have been unobserved thus far except for a detection of OH Meinel band emission by CRISM (Clancy et al., 2013). Hydrogen peroxide (H_2O_2) is a reservoir species that is formed by the recombination of 2 HO_2 radicals (R16) and is photolyzed during daytime (J8, J9). It has a lifetime of a few hours on
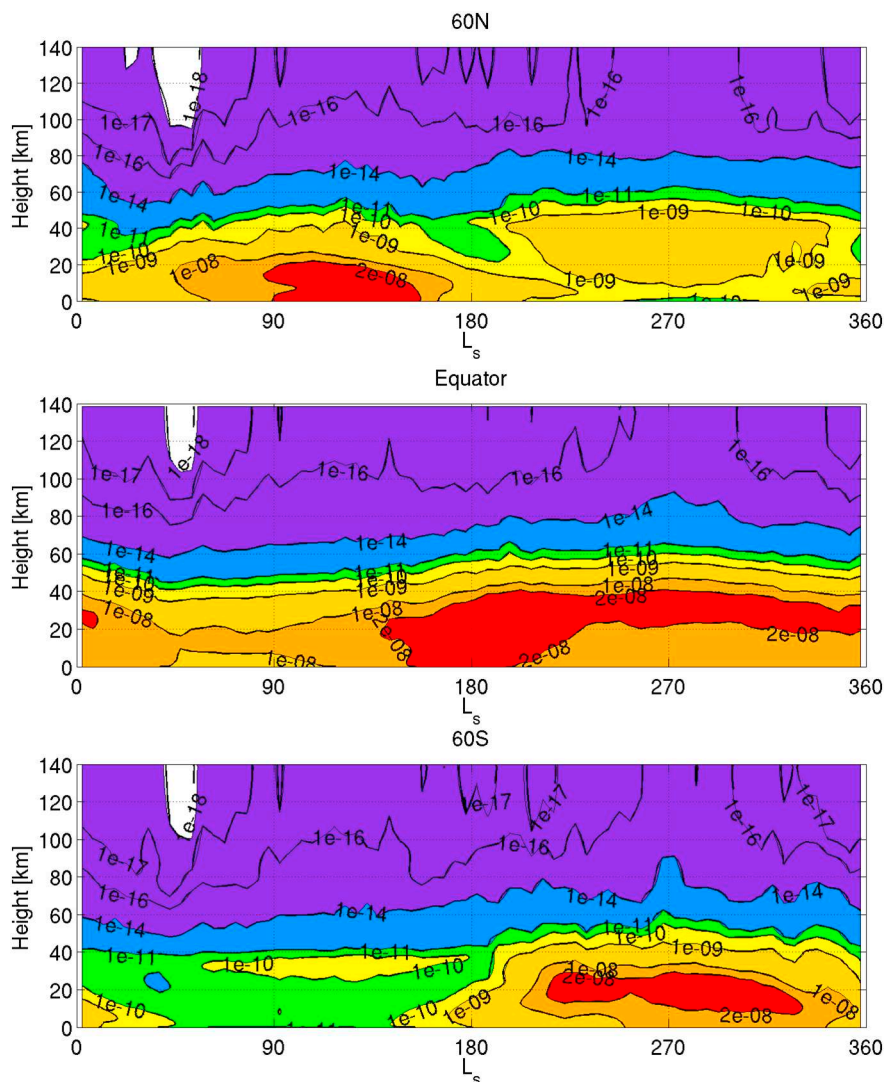
Fig. 21. Seasonal variation of the zonal mean H_2O_2 vmr vertical profile at 3 latitudes. The vmr was averaged over all longitudes and local times in 5° L_s bins.

Table 3
Overview of the available H_2O_2 observations and their latitudinal coverage. TEXES data taken from Encrenaz et al. (2012, 2015, 2017), JCMT data from Clancy et al. (2004), and HIFI/Herschell data from Hartogh et al. (2010).

Date	MY	L_s (°)	Observation	Latitude range	H_2O_2 (ppbv)
Feb. 2001	25	112	TEXES	20N–90N	< 6
June 2003	26	206	TEXES	20N	32 ± 10
Sept. 2003	26	250	JCMT	Full disk (center 20S)	18 ± 3
Nov.–Dec. 2005	27	332	TEXES	20S	15 ± 5
May–June 2008	28	80	TEXES	20N	10 ± 5
Oct. 2009	29	352	TEXES	20S	15
Apr. 2010	30	77	HIFI/Herschel	Full disk (center 20N)	< 2
March 2014	32	96	TEXES	50N	15 ± 7
July 2014	32	156	TEXES	30N	30 ± 7
May 2016	33	148	TEXES	30N	45 ± 10

the dayside (Lefèvre and Krasnopolsky, 2017) which makes it observable. The simulated H_2O_2 vertical columns and profiles, their spatial distribution and time evolution, are presented in various ways in Figs. 18, 19, 20, and 21.

H_2O_2 has been observed on several occasions with Earth-based telescopes (Clancy et al., 2004; Encrenaz et al., 2004, 2012, 2015). One attempted observation from space provided an upper limit (Hartogh et al., 2010). An overview of the available observations is given in Table 3 and Fig. 22. The first measurements from Mars orbit were presented in Aoki et al. (2015a, 2015b), the derived vmr were close to the detection limits, also the time resolution was coarse (seasonal averages).

Model results are added as follows. For every observation in Table 3, GEM-Mars H_2O_2 simulated columns relative to CO_2 columns were averaged in a 5 sol time window centered at the time of the observation for the latitude range given in Table 3. If only one latitude is given, a 10° latitude range around that value was considered. For full disk observations, an 80° latitude range was considered around the reported center. Only dayside output (SZA < 80°) was considered. The model reproduces the general trend of the observations. The model variability overlaps with all the observational error bars, except for 2 non-detections in the aphelion season, and also falls within the seasonal error bars derived in Aoki et al. (2015a, 2015b) (not shown). The mentioned non-detections remain puzzling. Previously it was found that heterogeneous chemistry processes on water ice clouds could account for a small decrease in the H_2O_2 columns around aphelion, but not enough to explain the non-detections (Encrenaz et al., 2015). Various model sensitivity tests (not shown) inform about uncertainties related to 1.
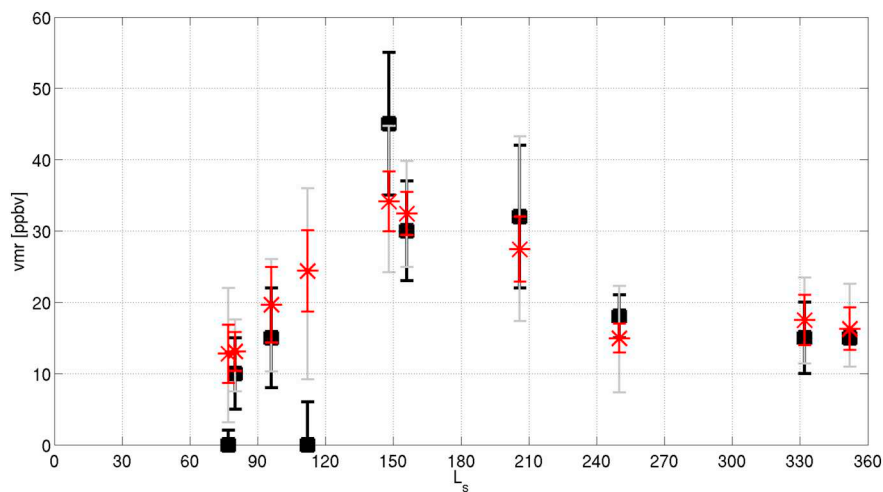
Fig. 22. H_2O_2 observations listed in Table 3 with their error bars (black) compared to GEM-Mars results (red) which were obtained as described in the text. Model error bars are 1 sigma variability (red) and full range (grey). (For interpretation of the references to color in this figure legend, the reader is referred to the web version of this article.)
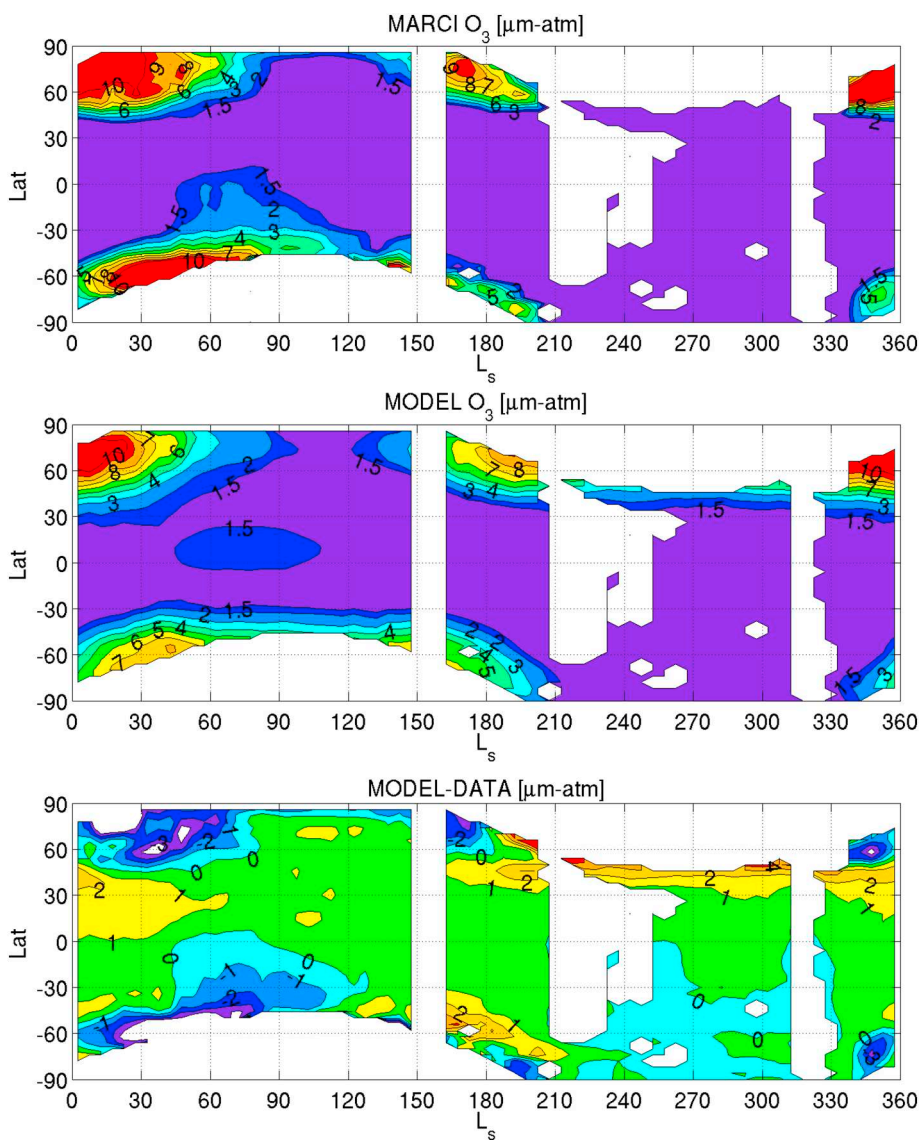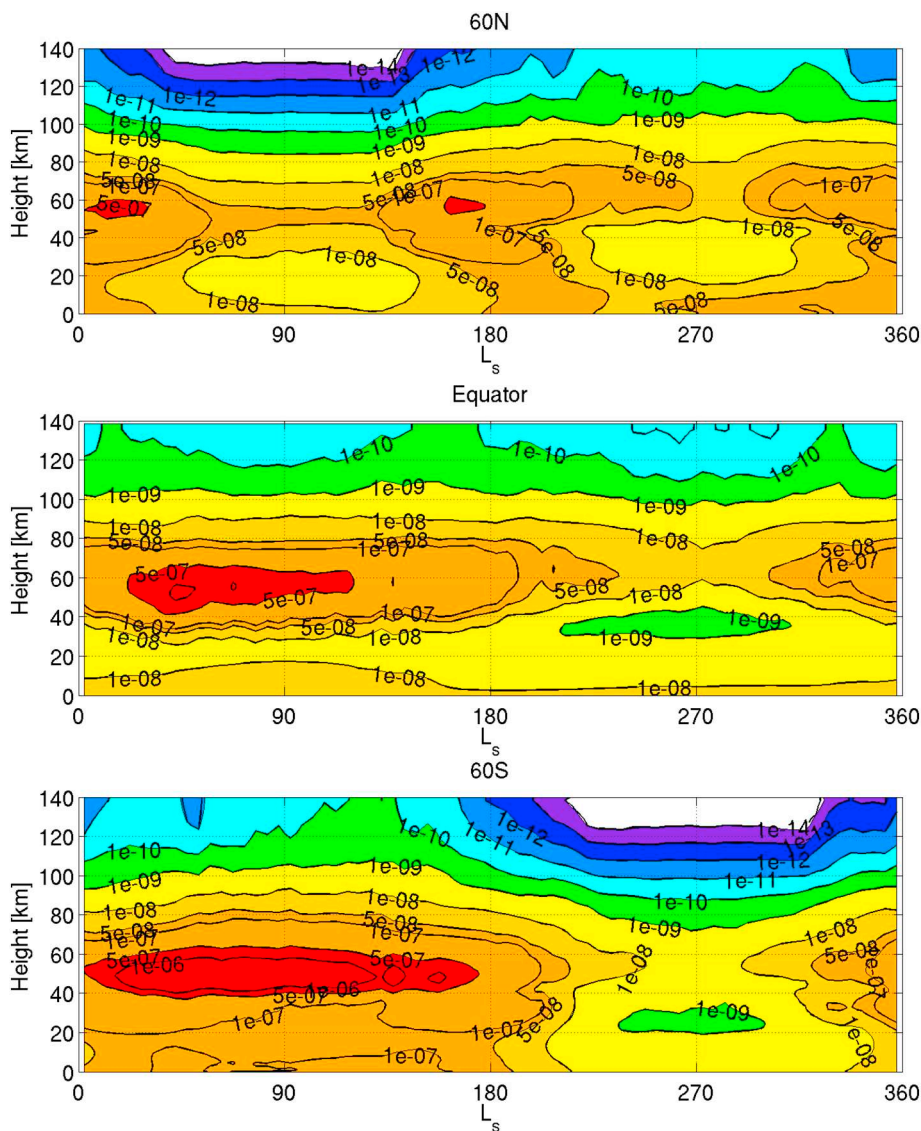

Fig. 23. Seasonal and latitudinal variation of the total vertical column abundance of O_3 observed by MARCI (Mars year 31, top) and simulated in the model (middle), and their difference (bottom). The model results are for daytime conditions (2–4 p.m., SZA < 80°). Data and model output were averaged over 5° L_s and 4° latitude bins. Model output was removed where no data was available or was contaminated by dust.
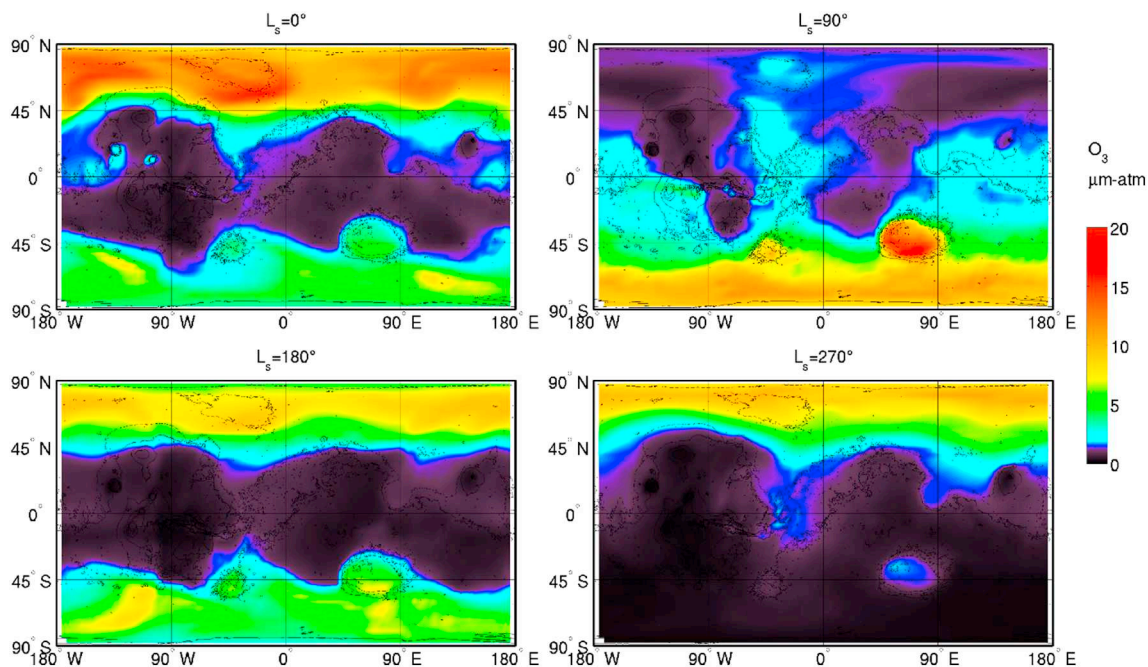
Fig. 24. Horizontal distribution of the total vertical column abundance of O_3 (in μm-atm) at the four cardinal seasons. See Fig. 9 for more details.
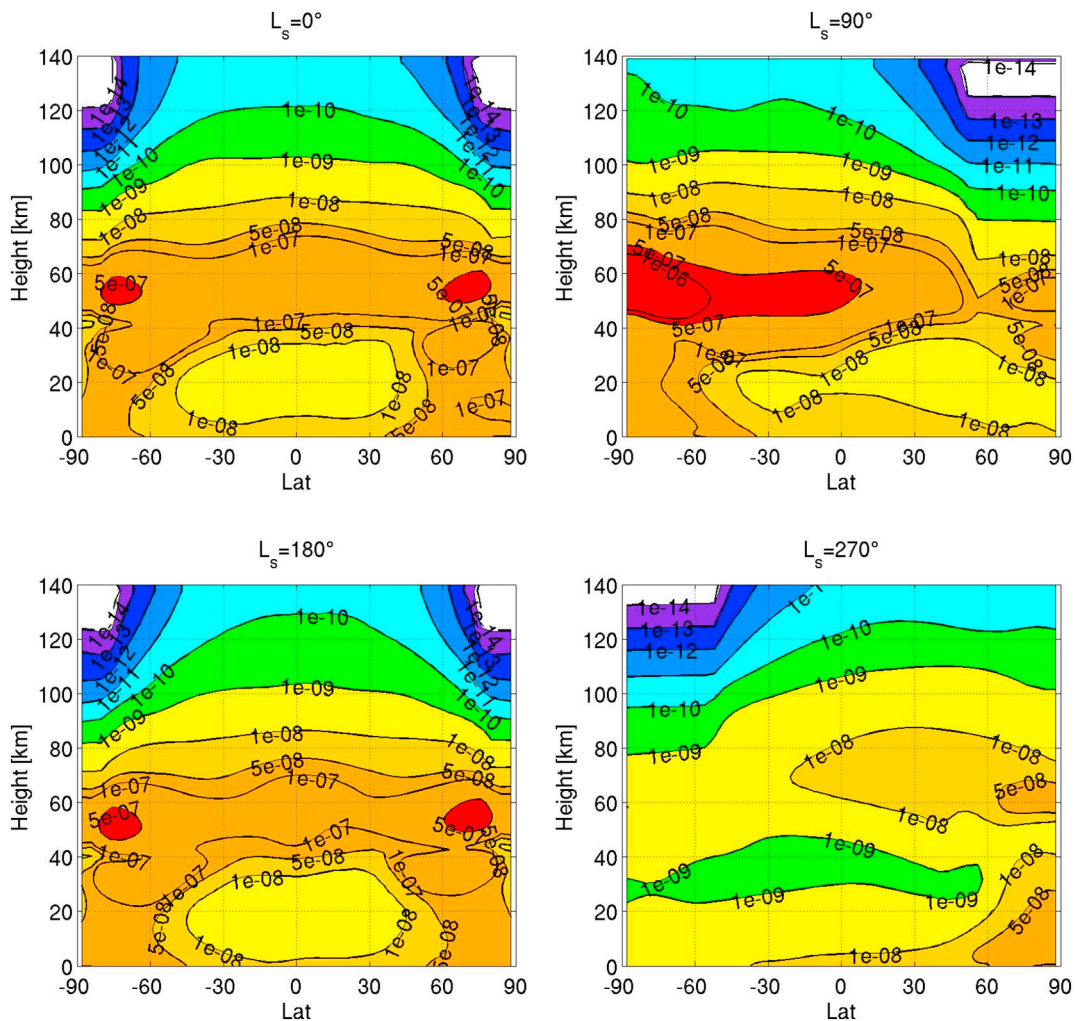
Fig. 25. Latitude-height zonal mean vertical distribution of the O_3 vmr for the four cardinal seasons. The vmr was averaged over all longitudes and local times and over 10 sols.

Fig. 26. Seasonal variation of the zonal mean O_3 vmr vertical profile at 3 latitudes. The vmr was averaged over all longitudes and local times in 5° L_s bins.

water abundances in the model, and 2. H_2O photolysis cross-sections, especially around 190 nm, leading to a variability of the simulated H_2O_2 abundances that is at least as large as that from heterogeneous chemistry as reported in Encrenaz et al. (2015).

3.6. Ozone

Ozone (O_3) is formed by the reaction of atomic (O) and molecular (O_2) oxygen in a 3-body reaction (R24). Both are photolysis products of CO_2 (J2, J3), and to a less extent H_2O (J13). O_3 is strongly photolyzed at daytime, either directly back into O_2 and O (J4) or through the excited state $O_2(a^1\Delta_g)$ (J14). This results in higher abundances of ozone in the polar nights (where ozone can be approximately considered as a passive tracer, e.g. Holmes et al. (2017)). Outside of the polar night, the day-night cycles are altitude dependent (García Muñoz et al., 2005). O_3 abundances are typically found in layers, usually a near surface layer where CO_2 abundances are maximal and the transmissivity limits ozone photolysis, and a layer just above the hygropause (e.g. Lefèvre et al. (2004), Montmessin and Lefèvre (2013)). The latter is caused by a strong anti-correlation between water vapor and ozone resulting from R11, which removes O atoms and suppresses R24, i.e. O_3 formation (Clancy and Nair, 1996). R11 is suppressed when water vapor

condenses out into ice.

Fig. 23 presents the comparison of the simulated total ozone column over one Mars year to the data from the MARs Color Imager (MARCI) on MRO for Mars year 31 (Clancy et al., 2016). Figs. 24, 25, and 26 show the horizontal and vertical distribution of ozone in similar views as for the other species discussed previously. In Fig. 23, the MARCI dataset consists of zonally and temporally averaged data over 1° latitude and 1° L_s. MARCI data are mainly taken between 2 and 4 p.m. local time, with some exceptions at polar latitudes, and the incident angle (SZA) is always below 80° (Clancy et al., 2016). Note that in the 2nd half of the year the MARCI retrievals are contaminated by dust (the most contaminated data were removed), and that MARCI O_3 retrievals showed little interannual variability (Clancy et al., 2016). Fig. 27 shows another comparison between MARCI and GEM-Mars simulated O_3 columns, averaged over latitude bands and L_s windows. Model-data differences are generally relatively small. Fig. 27 shows that the model is almost everywhere capable of matching the data within its full variability. The mean O_3 columns from the model in the respective intervals however sometimes deviate from the data. The MARCI O_3 column retrievals have a bottom sensitivity of ~1 μm-atm, which is particularly important for the very low values, where model-data biases of ~1 μm-atm may not be significant.
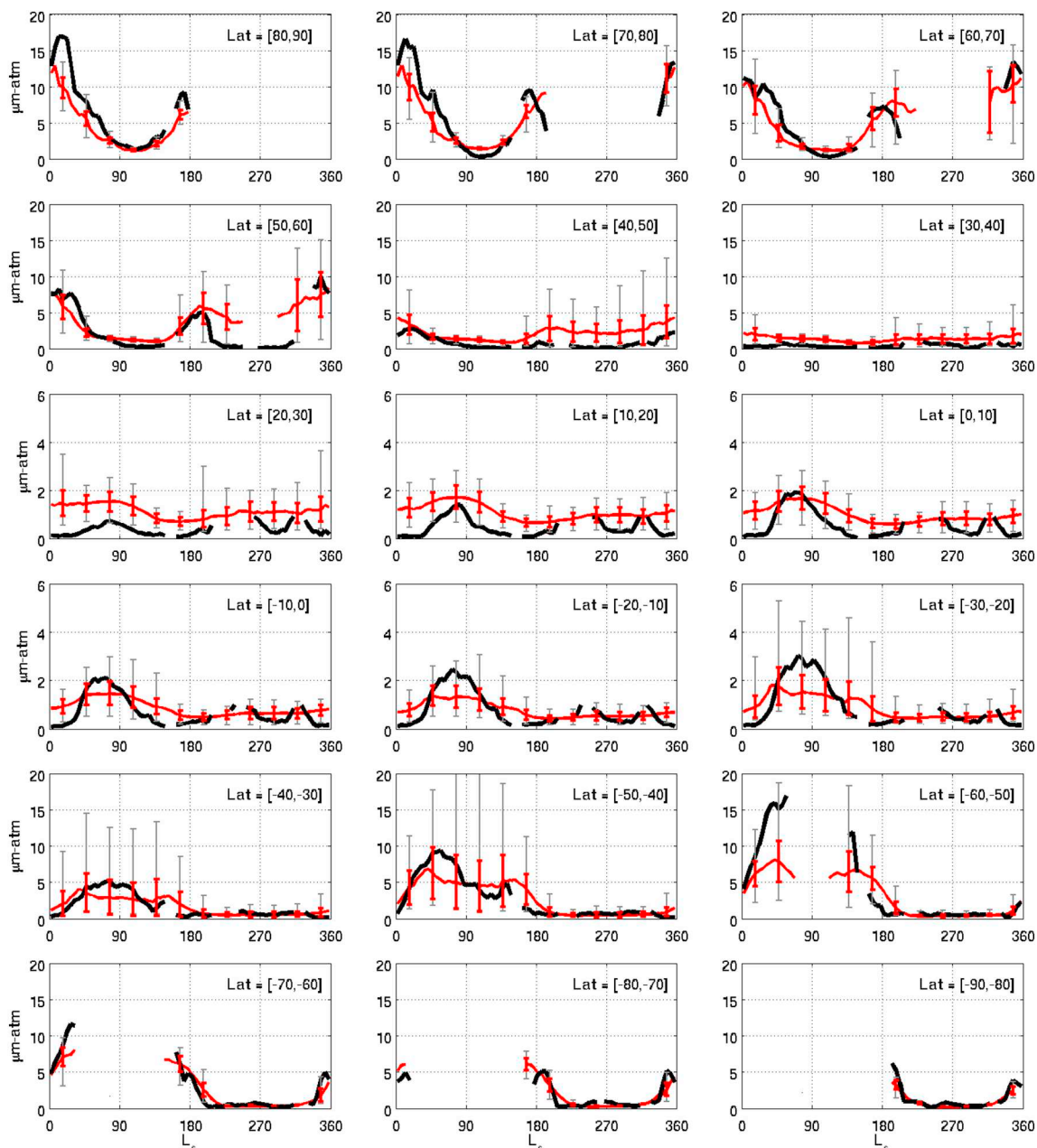
Fig. 27. Comparison of O_3 columns from MARCI (black) and GEM-Mars (red) averaged over 10° latitude bands and 5° L_s. Model averages contain only 14-16h local daytime (SZA < 80°) output. For visibility, model variability (error bars) is shown only for every 30° L_s. Red error bars are 1 sigma of the variability and grey error bars represent the full range. Note the difference in vertical scale for the various latitude intervals. (For interpretation of the references to color in this figure legend, the reader is referred to the web version of this article.)

In the first part of the year, roughly between $L_s \sim 30°$–90°, the model is underestimating O_3 columns both at high northern latitudes and at low southern latitudes. The same problem was already observed in the comparison of the LMD model with SPICAM observations (Lefèvre et al., 2008) and with MARCI observations (Clancy et al., 2016). Because of the apparent correlation with water ice clouds, this led Lefèvre et al. (2008) to include heterogeneous chemistry on water ice clouds to increase the model O_3. However, especially at low southern latitudes, the rates of heterogeneous reactions had to be considerably reduced, and the model-data bias appears already well before the maximum of the ACB. Comparisons to the more detailed MARCI dataset further weakened the support for heterogeneous chemistry (Clancy et al., 2016), although it cannot be entirely ruled out, especially at polar latitudes where the vertical distribution of water ice clouds is still weakly

constrained. But as these biases for O_3 coincide in time and place with the release of water vapor from northern subpolar latitudes, we expect rather that they are caused by an inaccurately simulated vertical distribution and transport of water vapor (which relates to water ice clouds, but not necessary includes heterogeneous chemistry). At high northern latitudes, the vertical transport of the released water vapor will be influenced by the presence of water ice clouds through condensation of water vapor, subsequent gravitational redistribution of water ice particles, and by radiative cloud effects affecting mixing and circulation. Also dust-induced vertical mixing can be expected to play a role in this season where strong ice-soil contrasts trigger local dust storms as the seasonal cap withdraws (Cantor et al., 2010; Daerden et al., 2015). The simplified cloud formation in the model including the absence of direct dust-cloud interactions, is likely to cause imperfect
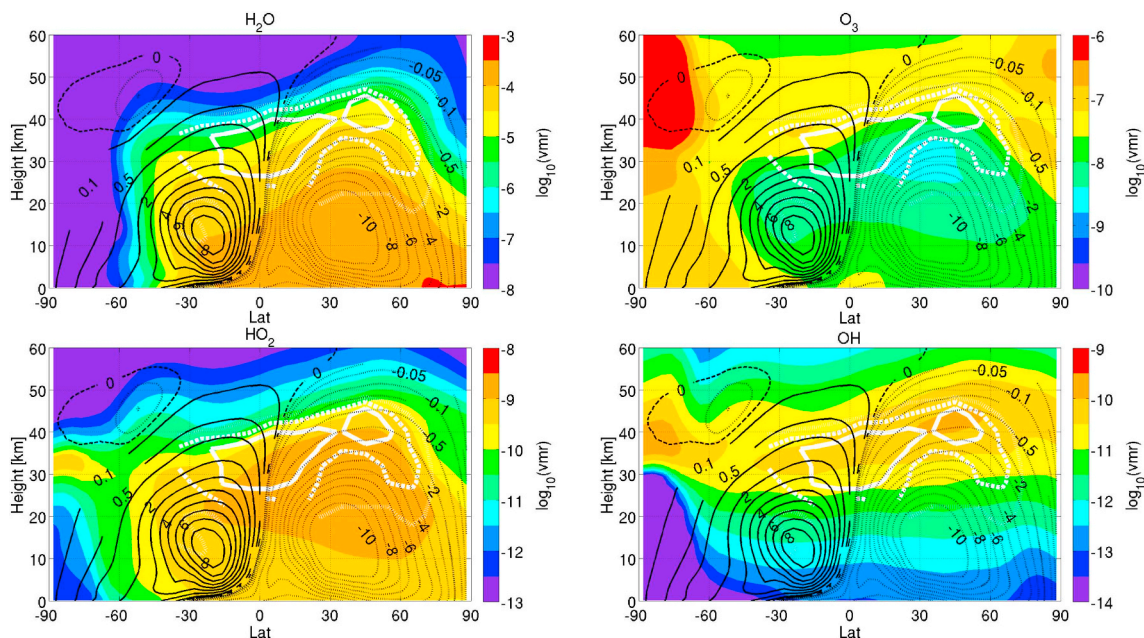
Fig. 28. Zonal mean daytime distribution of species (color) and the mass stream function ($\times 10^9$ kg/s, black contours) averaged over the period $L_s = 60°$–$100°$. Full lines represent counterclockwise movement, and dotted lines represent clockwise movement of air. The white contour lines are for the model/CRISM water vapor ratio of Fig. 15 for ratios of 10 (full), 5 (dashed) and 2 (dotted).

water vertical distributions that in turn have a direct impact on the ozone abundances. Fig. 15 shows an overestimation of water vapor in the model at latitude ~60°N between 15 and 35 km ($L_s = 30°$–$60°$) and up to 75°N between 25 and 40 km ($L_s = 60°$–$100°$). This is where the lower part of the O_3 layer is located (Figs. 25, 26), which contributes the most to the total column, given the exponential decay of air density. CRISM water vapor profiles are limited to altitudes above 10 (and sometimes 20) km, so no information on the accuracy of the water vapor profiles is known below those altitudes, where there may also be significant contributions to the total ozone columns. More refined and dense observations of the water vertical profile are needed in this area and season to further check how the model can be improved. We refer once more to the capability of the recently started TGO mission on vertical water profiling.

The excess of water in the model is most apparent in the equatorial region (Fig. 15). By assuming a simple scaling law between water vapor and ozone based on correlations between these species in the model, it was roughly estimated that the excessive water abundances cause a reduction in the ozone column of ~0.5 μm-atm in the equatorial region. This indicates that if the model would simulate more realistic water vapor abundances (compared to those from CRISM), this could indeed lead to a better simulation of the O_3 columns in the equatorial region around aphelion.

However, the low O_3 bias at southern mid-latitudes (Figs. 23, 27) cannot be explained by this. Indeed, the strong water excess in the model is limited to ~30°S (Fig. 15), while the O_3 column bias is larger for more southern latitudes. We conjecture that the high water vapor concentrations at ~40 km in the equatorial region cause an excess production of HO_x ($= HO_2 + OH$). A plot of the mean daytime mass stream function at the aphelion season (Fig. 28) shows that the global circulation passes through the region of excess water and moves air southwards during the daytime. This will also transport excessive HO_x southwards, where it causes a reduction in O_3 more strongly than in reality. Future simulations with either constraining of water vapor abundances or with an improved water cycle should test this theory.

At northern low to mid-latitudes (0°–40°N), $L_s \sim 0°$–$60°$, there is a small (in absolute value, $< \sim 1$ μm-atm) overestimation of the total O_3

columns, which has to be compared to the sensitivity of the MARCI retrievals of ~1 μm-atm, as well as other uncertainties in the retrievals (Clancy et al., 2016). Tests with Rayleigh scattering included (not shown) indicated that this would cause an additional decrease of ~10% in these northern low latitude O_3 columns. Similar biases are constrained to the edges of the polar nights (30°–70°N, $L_s \sim 150°$–$360°$, and 30°S–60°S, $L_s \sim 120°$–$210°$), where model resolution effects play a role. The model imposes a resolution of 4° on the SZA, but also has an influence on the dynamical isolation of the polar vortex (Daerden et al., 2007), which may explain why the O_3 bias extends further from the polar night's edge than 4° latitude.

Nighttime vertical O_3 profiles were obtained from the SPICAM stellar occultation measurements (Lebonnois et al., 2006). While these data could be applied to further evaluate the model, the dataset is currently being reviewed and extended (S. Lebonnois, A. Määttänen, private communications) and was not available yet at the submission of this paper. However, our simulations compare well to some early results presented in Montmessin and Lefèvre (2013). The NOMAD instrument (Vandaele et al., 2018) on TGO will provide O_3 vertical profiles with unprecedented vertical resolution and vertical coverage, nearly simultaneously with H_2O profiles. This dataset is expected to provide important information to further improve models.

3.7. Oxygen dayglow

During the daytime, $O_2(a^1\Delta_g)$ is formed in the lower atmosphere of Mars by photolysis of ozone (reaction J14). Excitation through 3-body recombination (R31) contributes negligibly in these conditions. Within the lowest scale height (~10 km), the destruction of $O_2(a^1\Delta_g)$ is dominated by quenching (collisional de-excitation, reaction R30), but above this, radiative relaxation (J15) causes dayglow at 1.27 μm. As a result, $O_2(a^1\Delta_g)$ dayglow is a proxy of daytime O_3 concentrations (Noxon et al., 1976, Fedorova et al., 2006, Guslyakova et al., 2016, Clancy et al., 2017).

The volume emission rate (VER) of the $O_2(a^1\Delta_g)$ 1.27 μm dayglow is calculated in the model from the $O_2(a^1\Delta_g)$ vmr by multiplying by the air number density and the rate of reaction J15, 2.237×10^{-4} s^{-1}. Here
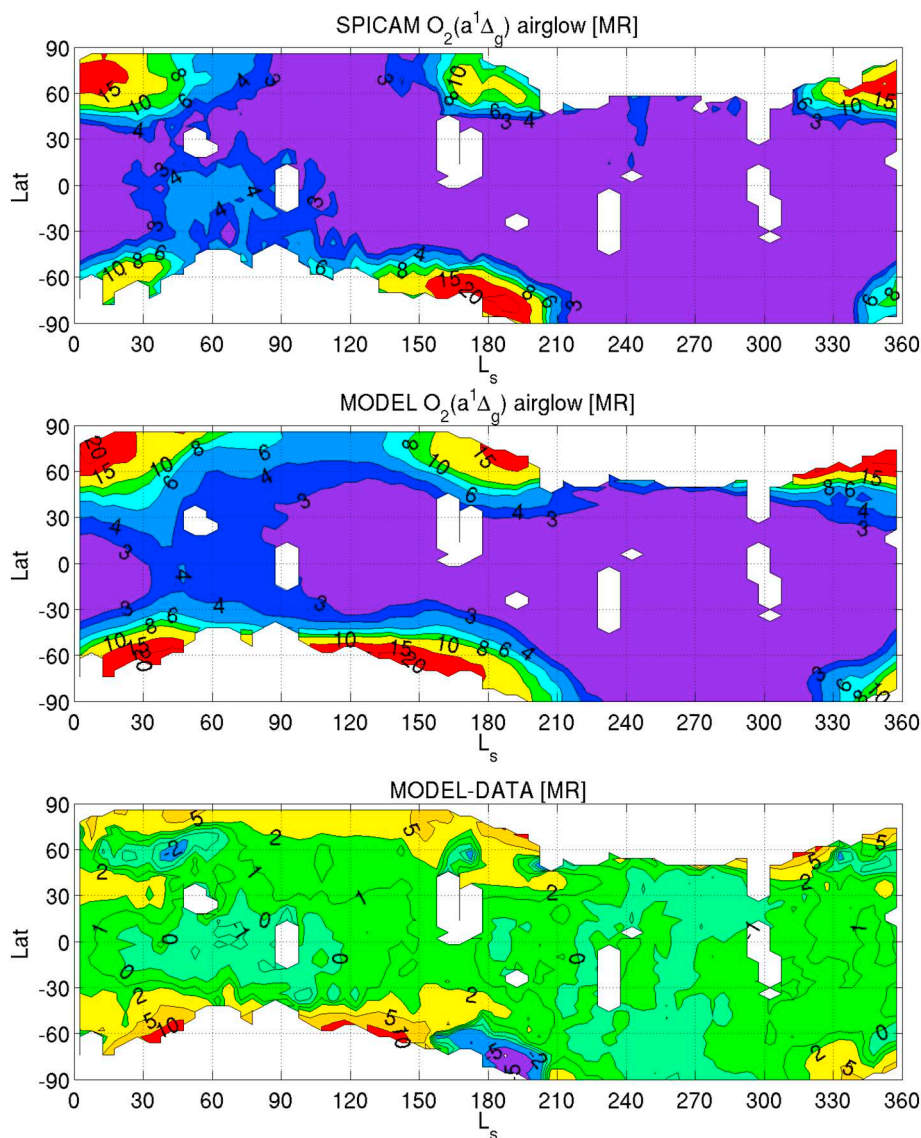
Fig. 29. Seasonal and latitudinal variation of the vertically integrated $O_2(a^1\Delta_g)$ 1.27 µm dayglow emission observed by SPICAM (Mars years 26, 27, 29–32, top) and simulated in the model (middle), and their difference (bottom). Units are mega-Rayleigh (MR). The model results are for daytime conditions (SZA < 80°). Data and model output were averaged over 5° L_s and 4° latitude bins. Model output was removed where no data was available.

we compare the total vertically integrated dayglow emission to the observations by SPICAM on Mars Express (Guslyakova et al., 2016), see Fig. 29. In addition, Figs. 30, 31 and 32 show the horizontal and vertical distribution of the airglow emission, and Fig. 33 shows a more detailed model-data comparison in 10° latitude bands. Data from 5 Mars years (26 to 32, but excluding 28 during which a global dust storm occurred, which we will not consider in this paper) were combined and averaged in L_s and latitude bins. GEM-Mars dayglow emission was averaged over the entire daytime region (SZA < 80°). Because the attenuation due to dust and water ice clouds was not included in the retrieval (Guslyakova et al., 2016), we present model results that include the attenuation in the calculation of the emission rates (see Section 2.2). The general patterns are well reproduced. As $O_2(a^1\Delta_g)$ is a proxy for O_3, the model-data biases are often similar to the case for O_3, and the same analysis of their nature can be made (Section 3.6). Differences can be attributed to the different altitude dependence of O_3 and airglow, with airglow being more dominated by the lower altitudes compared to O_3 (see Figs. 25, 26, 31 and 32). Another important factor at play is the difference in local time of the observations, where MARCI

observations are done at ~3 p.m. local time, the range in local times for SPICAM is much broader (Guslyakova et al., 2016).

4. Conclusions

GEM-Mars is a general circulation model for the Martian atmosphere from the surface up to ~150 km. It contains a range of parameterizations for physical processes and includes a fully online atmospheric chemistry calculation. At present 16 tracers for atmospheric gases are included, of which 13 are chemically active. The current atmospheric chemistry contains the photolysis of the main constituent, CO_2, and of H_2O, and of their photolysis products and their mutual gasphase interactions. As such this represents the basic picture of the chemical composition of Martian atmosphere as it is known today. GEM-Mars is the second Mars GCM with atmospheric chemistry and provides an opportunity for inter model comparisons and for improved understanding of the chemistry on Mars. GEM-Mars is also a core GCM model applied for the analysis and interpretation of data from the NOMAD spectrometer on the ESA-Roskosmos ExoMars Trace Gas
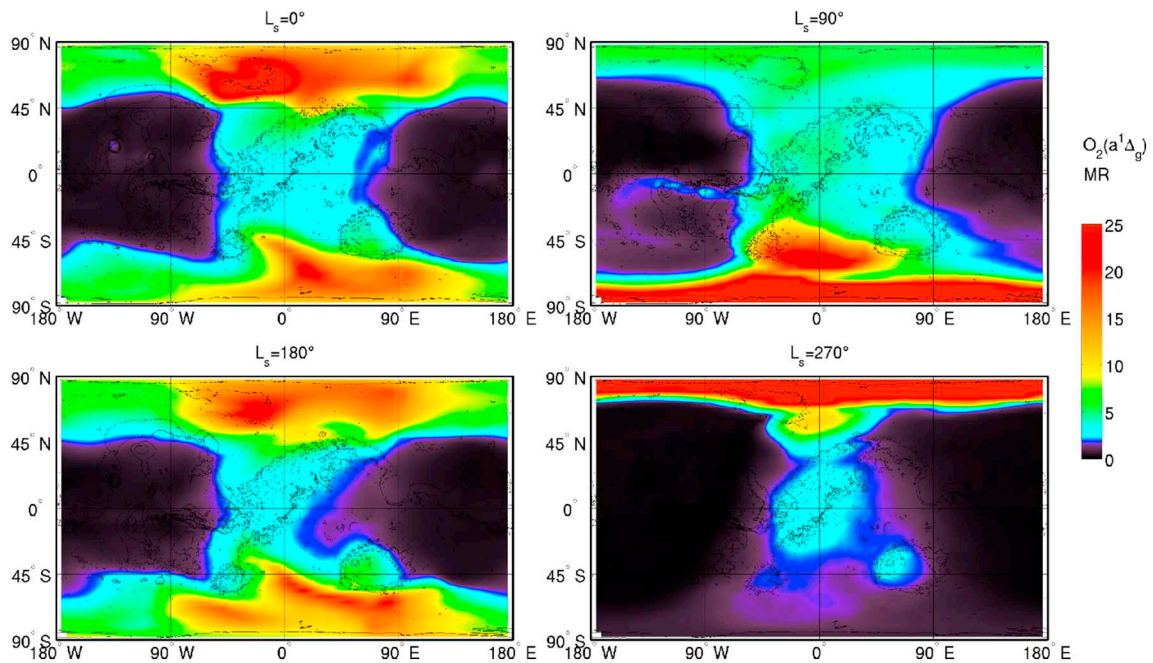
Fig. 30. Horizontal distribution of the vertically integrated $O_2(a^1\Delta_g)$ 1.27 μm dayglow emission (in MR) at the four cardinal seasons. See Fig. 9 for more details.
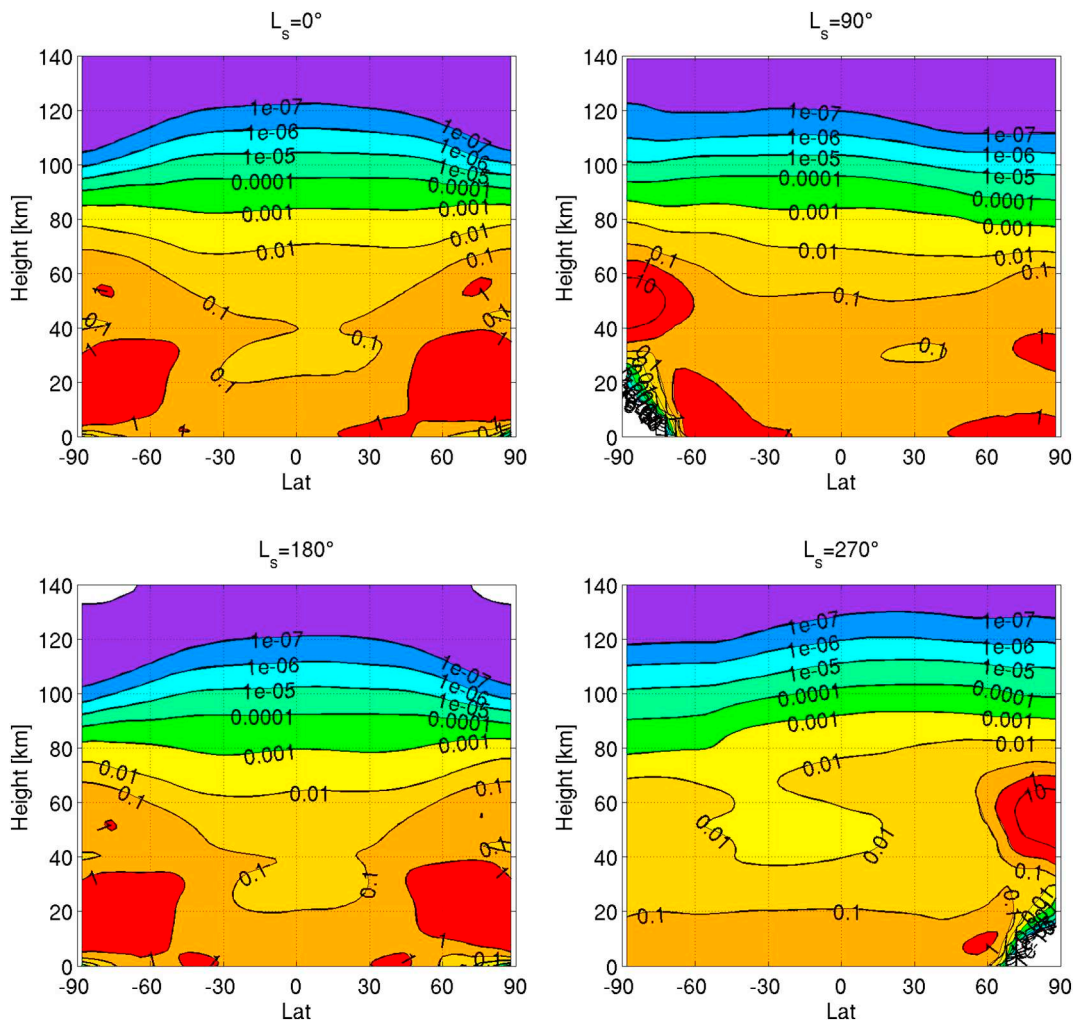

Fig. 31. Latitude-height zonal mean vertical distribution of the $O_2(a^1\Delta_g)$ volume emission rate (VER, in 10^{12} photons m^{-3} s^{-1}) for the four cardinal seasons. The VER was averaged over all longitudes (and local times) and over 10 sols.
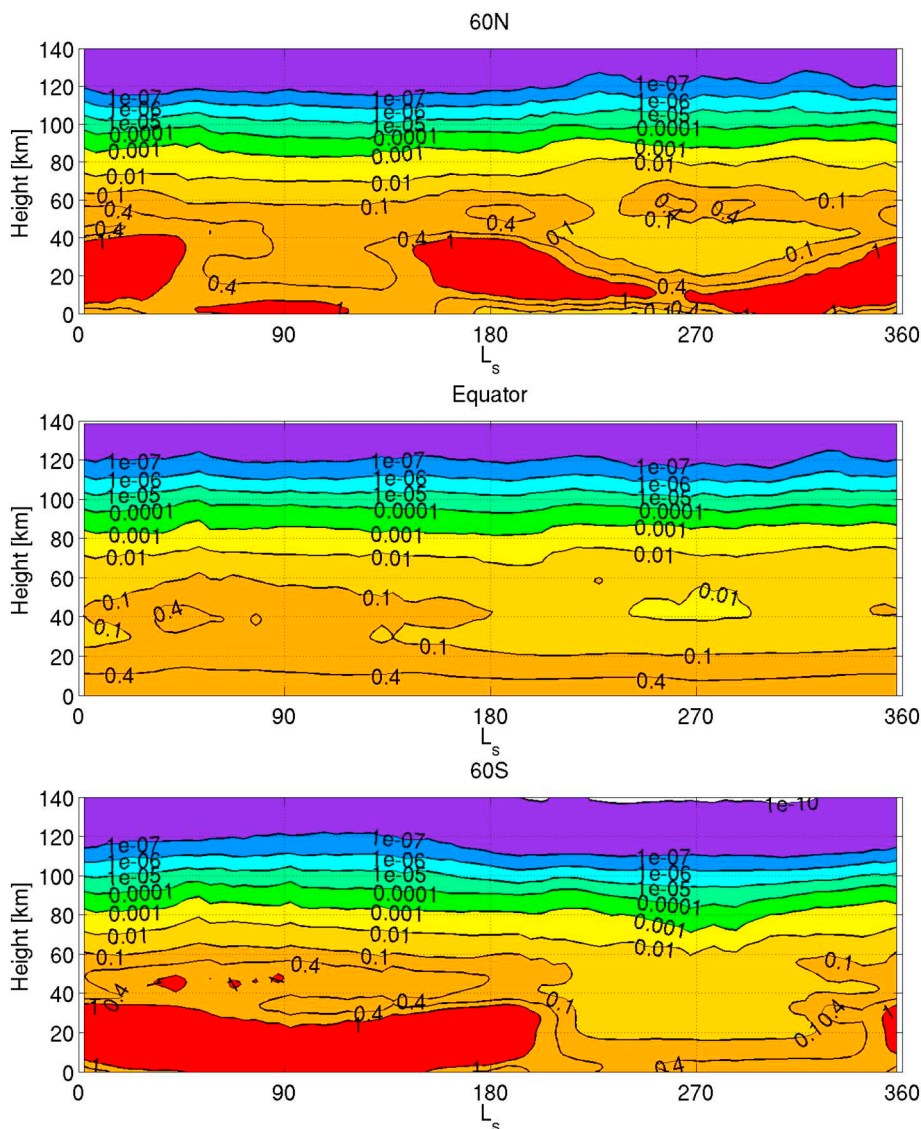
Fig. 32. Seasonal variation of the zonal mean $O_2(a^1\Delta_g)$ VER (in 10^{12} photons $m^{-3} s^{-1}$) vertical profile at 3 latitudes. The VER was averaged over all longitudes and local times in $5°$ L_s bins.

Orbiter (Vandaele et al., 2018; Korablev et al., 2018).

The present paper is a follow-up of the general model description and evaluation paper Neary and Daerden (2018) and focuses on the atmospheric chemistry simulations in GEM-Mars. Comparisons are presented to some of the most extended global and (multi-)annual observations of vertically integrated CO, H_2O (both of which were presented in more detail in previous publications), O_3, and $O_2(a^1\Delta_g)$ 1.27 μm dayglow, as well as to the full available dataset of H_2O_2 observations. The general performance of the model is consistent with the observations, and the remaining model-data biases provide information on processes that are not well represented in the model.

The GEM-Mars model simulation reproduces almost all the available H_2O_2 observations within its variability and the observational error bars (except for two outliers that remain puzzling). This is a strong and encouraging result, as H_2O_2 is an important reservoir species in the main photochemical cycles. For O_3, the biases are consistent with those found in other model studies (Clancy et al., 2016). It was found that the most important biases for O_3 are most likely related to the vertical distribution of water vapor, a conclusion consistent with that of Clancy et al. (2017). The limited availability of observations of the vertical profile of water vapor in the lower and middle atmosphere complicates an in-depth analysis. But the available (derived) data confirm a

correlation between an overestimation of mid-atmospheric water abundances and underestimation of ozone columns in the model at aphelion low southern latitudes and northern high latitudes. The low latitude water bias is related to excessive heating of water ice clouds in the ACB, which is caused by the currently simplistic cloud scheme in GEM-Mars. At northern high latitudes in springtime, the bias may also be related to dust-induced mixing. The problem is notably related to ozone and oxygen airglow, because these appear in atmospheric layers that contribute significantly to the total column abundance, and are located just above the hygropause. As a result, small changes in the vertical water distribution can readily affect the total column abundances. H_2O_2 column abundances are less dependent on this as this species is more confined to the lower atmosphere.

More refined cloud microphysics, including dust-cloud interactivity, is required for an improved simulation of the water vapor vertical profile, which controls the atmospheric chemistry. A detailed microphysical model was developed (Daerden et al., 2010) and is currently being implemented. Other model developments in progress, in attendance of the observations by the Trace Gas Orbiter mission, include the inclusion of HDO and D/H fractionation, and methane- and nitrogen chemistry.
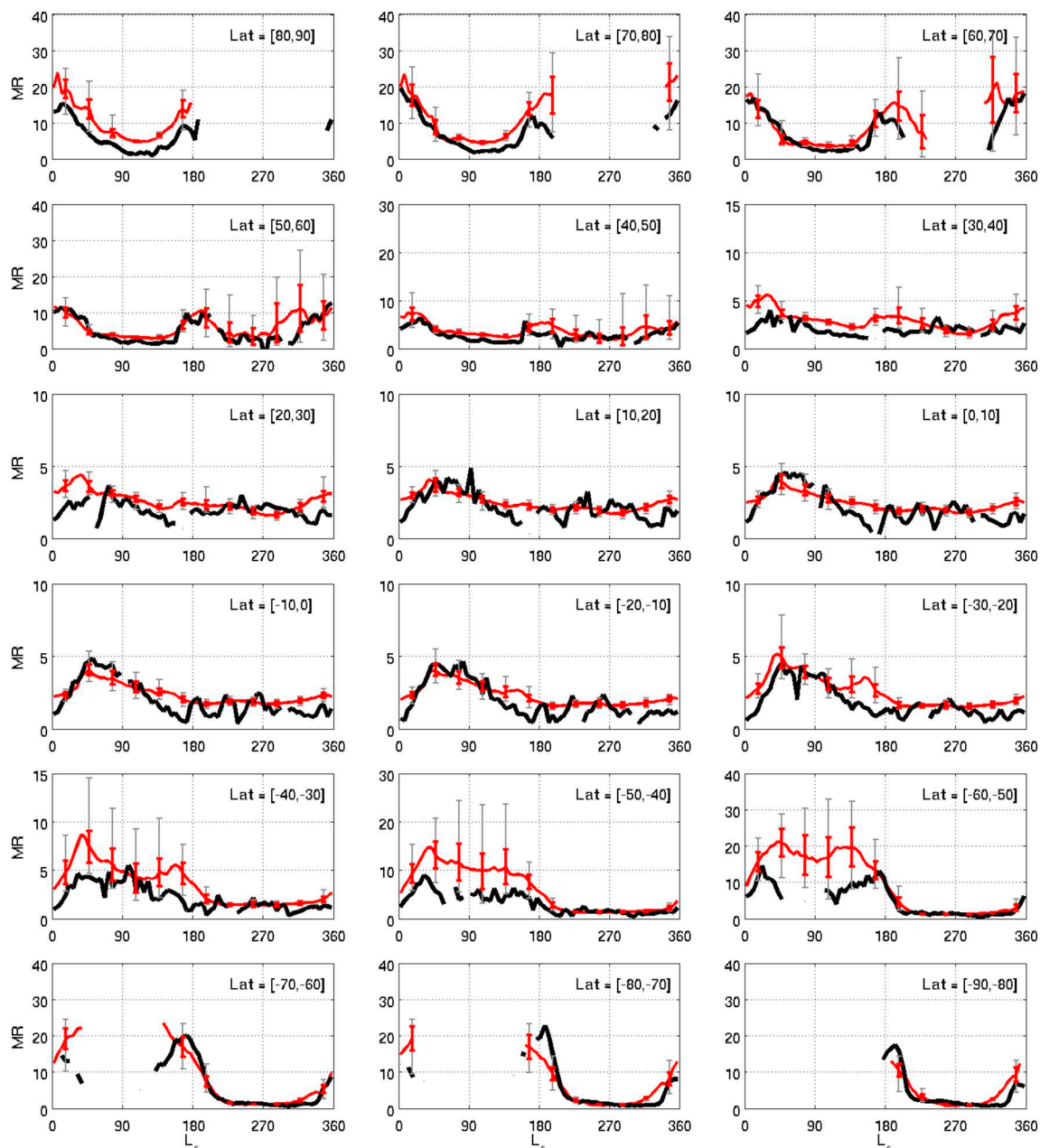
Fig. 33. Comparison of $O_2(a^1\Delta_g)$ vertically integrated dayglow emissions from SPICAM (black) and GEM-Mars (red), averaged over 10° latitude bands and 5° L_s. Figure set-up as in Fig. 27. SPICAM data were combined for Mars years 26, 27, 29–32. (For interpretation of the references to color in this figure legend, the reader is referred to the web version of this article.)

References

Akingunola, A., 2008. Martian water cycle modeling with the second generation of the global Mars multiscale model, PhD thesis. In: York Univ. Toronto, Canada.

Allison, M., 1997. Accurate analytic representations of solar time and seasons on Mars with applications to the Pathfinder/Surveyor missions. Geophys. Res. Lett. 24 (16), 1967–1970.

Allison, M., McEwen, M., 2000. A post-Pathfinder evaluation of areocentric solar coordinates with improved timing recipes for Mars seasonal/diurnal climate studies. Planet. Sp. Sci. 48, 215–235.

Aoki, S., Giuranna, M., Kasaba, Y., Nakagawa, H., Sindoni, G., Geminale, A., Formisano, V., 2015a. Search for hydrogen peroxide in the Martian atmosphere by the Planetary Fourier Spectrometer onboard Mars Express. Icarus 245, 177–183. https://doi.org/10.1016/j.icarus.2014.09.034.

Aoki, S., Nakagawa, H., Sagawa, H., Giuranna, M., Sindoni, G., Aronica, A., Kasaba, Y., 2015b. Seasonal variation of the HDO/H$_2$O ratio in the atmosphere of Mars at the middle of northern spring and beginning of northern summer. Icarus 260, 7–22. https://doi.org/10.1016/j.icarus.2015.06.021.

Atreya, S.K., Mahaffy, P.R., Wong, A.S., 2007. Methane and related trace species on Mars: origin, loss, implications for life, and habitability. Planet. Sp. Sci. 55, 358–369. https://doi.org/10.1016/j.pss.2006.02.005.

Barker, E.S., 1972. Detection of molecular oxygen in the Martian atmosphere. Nature 238, 447–448.

Barth, C.A., Hord, C.W., 1971. Mariner 6 and 7 ultraviolet spectrometer experiment: topography and polar cap. Science 173, 197–201.

Brasseur, G., Solomon, S., 2005. Aeronomy of the Middle Atmosphere. Springer, Verlag.

Burkholder, J.B., et al., 2015. Chemical kinetics and photochemical data for use in atmospheric studies, Evaluation no. 18, JPL publication 15-10, Jet Propulsion Laboratory. Pasadena 2015. http://jpldataeval.jpl.nasa.gov.

Cantor, B.A., James, P.B., Calvin, W.M., 2010. MARCI and MOC observations of the atmosphere and surface cap in the north polar region of Mars. Icarus 208, 61–81. https://doi.org/10.1016/j.icarus.2010.01.032.

Carleton, N.P., Traub, W.A., 1972. Detection of molecular oxygen on Mars. Science 177, 988–992.

Chipperfield, M.P., Cariolle, D., Simon, P., Ramaroson, R., Lary, D.J., 1993. A 3-dimensional modeling study of trace species in the Arctic lower stratosphere during winter 1989–1990. J. Geophys. Res. 98, 7199–7218.

Chung, C.-Y., Chew, E.P., Cheng, B.-M., Bahou, M., Lee, Y.-P., 2001. Temperature dependence of absorption cross-section of H$_2$O, HOD, and D$_2$O in the spectral region 140–193 nm. Nucl. Instr. Meth. Phys. Res. A 467-468, 1572–1576.

Clancy, R.T., Nair, H., 1996. Annual (perihelion–aphelion) cycles in the photochemical behavior of the global Mars atmosphere. J. Geophys. Res. 101, 12785–12790.

Clancy, R.T., Sandor, B.J., García-Muñoz, A., Lefèvre, F., Smith, M.D., Wolff, M.J., Montmessin, F., Murchie, S.L., Nair, H., 2013. First detection of Mars atmospheric hydroxyl: CRISM Near-IR measurement versus LMD GCM simulation of OH Meinel band emission in the Mars polar winter atmosphere. Icarus 226, 272–281. https://doi.org/10.1016/j.icarus.2013.05.035.

Clancy, R.T., Sandor, B.J., Moriarty-Schieven, G.H., 2004. A measurement of the 362 GHz absorption line of Mars atmospheric H$_2$O$_2$. Icarus 168, 116–121.

Clancy, R.T., Smith, M.D., Lefèvre, F., McConnochie, T.H., Sandor, B.J., Wolff, M.J., Lee, S.W., Murchie, S.L., Toigo, A.D., Nair, H., Navarro, T., 2017. Vertical profiles of Mars 1.27 μm O$_2$ dayglow from MRO CRISM limb spectra: seasonal/global behaviors, comparisons to LMDGCM simulations, and a global definition for Mars water vapor profiles. Icarus 293, 132–156. https://doi.org/10.1016/j.icarus.2017.04.011.

Clancy, R.T., Wolff, M.J., Lefèvre, F., Cantor, B.A., Malin, M.C., Smith, M.D., 2016. Daily global mapping of Mars ozone column abundances with MARCI UV band imaging. Icarus 266, 112–133. https://doi.org/10.1016/j.icarus.2015.11.016.

Clancy, R. T., et al. (2012), Extensive MRO CRISM observations of 1.27 mm O$_2$ airglow in Mars polar night and their comparison to MRO MCS temperature profiles and LMD GCM simulations, J. Geophys. Res., 117, E00J10, doi:https://doi.org/10.1029/2011JE004018.

Côté, J., Gravel, S., Méthot, A., Patoine, A., Roch, M., Staniforth, A., 1998a. The operational CMC–MRB Global Environmental Multiscale (GEM) Model. Part I: Design considerations and formulation. Mon. Wea. Rev. 126 (6), 1373–1395.

Côté, J., Desmarais, J.-G., Gravel, S., Méthot, A., Patoine, A., Roch, M., Staniforth, A., 1998b. The operational CMC-MRB global environmental multiscale (GEM) model. Part II: Results. Mon. Wea. Rev. 126, 1397–1418.

Daerden, F., Larsen, N., Chabrillat, S., Errera, Q., Bonjean, S., Fonteyn, D., Hoppel, K., Fromm, M., 2007. A 3D-CTM with detailed online PSC-microphysics: analysis of the Antarctic winter 2003 by comparison with satellite observations. Atmos. Chem. Phys. 7, 1755–1772.

Daerden, F., Whiteway, J.A., Davy, R., Verhoeven, C., Komguem, L., Dickinson, C., Taylor, P.A., Larsen, N., 2010. Simulating observed boundary layer clouds on Mars. Geophys. Res. Lett. 37, L04203. https://doi.org/10.1029/2009GL041523.

Daerden, F., Whiteway, J.A., Neary, L., Komguem, L., Lemmon, M.T., Heavens, N.G., Cantor, B.A., Hébrard, E., Smith, M.D., 2015. A solar escalator on Mars: self-lifting of dust layers by radiative heating. Geophys. Res. Lett. 42, 73197326. https://doi.org/10.1002/2015GL064892.

Encrenaz, T., Bézard, B., Greathouse, T.K., Richter, M.J., Lacy, J.H., Atreya, S.K., Wong, A.S., Lebonnois, S., Lefèvre, F., Forget, F., 2004. Hydrogen peroxide on Mars: evidence for spatial and temporal variations, Icarus 170, 424–429.

Encrenaz, T., Greathouse, T.K., Lefèvre, F., Atreya, S.K., 2012. Hydrogen peroxide on Mars: observations, interpretation and future plans. Planet. Sp. Sci. 68, 3–17. https://doi.org/10.1016/j.pss.2011.03.019.

Encrenaz, T., Greathouse, T.K., Lefèvre, F., Montmessin, F., Forget, F., Fouchet, T., DeWitt, C., Richter, M.J., Lacy, J.H., Bézard, B., Atreya, S.K., 2015. Seasonal variations of hydrogen peroxide and water vapor on Mars: further indications of heterogeneous chemistry. Astron. Astrophys. 578, A127. https://doi.org/10.1051/0004-6361/201425448.

Encrenaz, T., DeWitt, C., Richter, M.J., Greathouse, T.K., Fouchet, T., Montmessin, F., Lefèvre, F., Forget, F., Bézard, B., Atreya, S.K., Case, M., Ryde, N., 2016. A map of D/H on Mars in the thermal infrared using EXES aboard SOFIA. Astron. Astrophys. 586, A62. https://doi.org/10.1051/0004-6361/201527018.

Encrenaz, T., Greathouse, T.K., Lefèvre, F., Montmessin, F., Fouchet, T., Bézard, B., Atreya, S.K., Gondet, B., Fedorova, A., Hartogh, P., 2017. Seasonal and interannual variations of H$_2$O$_2$ on Mars, European Planetary Science Congress 2017, held 17-22 September, 2017 in Riga, Latvia, id. In: EPSC2017–175.

Encrenaz, T., DeWitt, C., Richter, M.J., Greathouse, T.K., Fouchet, T., Montmessin, F., Lefèvre, F., Bézard, B., Atreya, S.K., Aoki, S., Sagawa, H., 2018. New measurements of D/H on Mars using EXES aboard SOFIA. Astron. Astrophys. 612, A112. https://doi.org/10.1051/0004-6361/201732367.

Etiope, G., 2018. Understanding the origin of methane on Mars through isotopic and molecular data from the ExoMars orbiter. Planet. Sp. Sci. 159, 93–96. https://doi.org/10.1016/j.pss.2018.04.020.

Fazel-Rastgar, F., 2016. South polar permanent CO$_2$ ice cap presentation in the Global Mars Multiscale Model. Adv. Sp. Res. 61, 1170–1180.

Fedorova, A., Bertaux, J.-L., Betsis, D., Montmessin, F., Korablev, O., Maltagliati, L., Clarke, J., 2018. Water vapor in the middle atmosphere of Mars during the 2007 global dust storm. Icarus 300, 440–457. https://doi.org/10.1016/j.icarus.2017.09.025.

Fedorova, A., Korablev, O., Perrier, S., Bertaux, J.-L., Lefèvre, F., Rodin, A., 2006. Observation of O$_2$ 1.27 mm dayglow by SPICAM IR: seasonal distribution for the first Martian year of Mars Express. J. Geophys. Res. 111, E09S07. https://doi.org/10.1029/2006JE002694.

Forget, F., Hourdin, F., Fournier, R., Hourdin, C., Talagrand, O., Colins, M., Lewis, S.R., Read, P.L., Huot, J.P., 1998. CO$_2$ snowfall on Mars: Simulation with a General Circulation Model. Icarus 131, 302–316.

Franz, H.B., Trainer, M.G., Wong, M.H., Mahaffy, P.R., Atreya, S.K., Manning, H.L.K., Stern, J.C., 2015. Reevaluated martian atmospheric mixing ratios from the mass spectrometer on the Curiosity rover. Planet. Sp. Sci. 109-110, 154–158. https://doi.org/10.1016/j.pss.2015.02.014.

Gagné, M.-È., Melo, S.M.L., Lefèvre, F., González-Galindo, F., Strong, K., 2012. Modeled O$_2$ airglow distributions in the Martian atmosphere. J. Geophys. Res. 117, E06005. https://doi.org/10.1029/2011JE003901.

García Muñoz, A., McConnell, J.C., McDade, I.C., Melo, S.M.L., 2005. Airglow on Mars: Some model expectations for the OH Meinel bands and the O2 IR atmospheric band. Icarus 176, 75–95. https://doi.org/10.106/j.icarus.2005.01.006.

Greybush, S.J., Wilson, R.J., Hoffman, R.N., Hoffman, M.J., Miyoshi, T., Ide, K., McConnochie, T., Kalnay, E., 2012. Ensemble Kalman filter data assimilation of thermal emission spectrometer temperature retrievals into a Mars GCM. J. Geophys. Res. 117, E11008. https://doi.org/10.1029/2012JE004097.

Guslyakova, S., Fedorova, A., Lefèvre, F., Korablev, O., Montmessin, F., Trokhimovskiy, A., Bertaux, J.-L., 2016. Long-term nadir observations of the O 2 dayglow by SPICAM IR. Planet. Sp. Sci. 122, 1–12. https://doi.org/10.1016/j.pss.2015.12.006.

Haberle, R.M., Clancy, R.T., Forget, F., Smith, M.D., Zurek, R.W. (Eds.), 2017. The Atmosphere and Climate of Mars. Press, Cambridge University.

Hartogh, P., Jarchow, C., Lellouch, E., et al., 2010. Herschel/HIFI observations of Mars: first detection of O$_2$ at submillimetre wavelengths and upper limits on HCl and H$_2$O$_2$. Astron. Astrophys. 521, L49. https://doi.org/10.1051/0004-6361/201015160.

Hitchcock, D.R., Lovelock, J.E., 1967. Life detection by atmospheric analysis. Icarus 7, 149–159.

Holmes, J.A., Lewis, S.R., Patel, M.R., 2017. On the link between martian total ozone and potential vorticity. Icarus 282, 104–117. https://doi.org/10.1016/j.icarus.2016.10.004.

Ityaksov, D., Linnartz, H., Ubachs, W., 2008. Deep-UV absorption and Rayleigh scattering of carbon dioxide. Chem. Phys. Lett. 462, 31–34.

Jakosky, B.M., Farmer, C.B., 1982. The seasonal and global behavior of water vapor in the Martian atmosphere: complete global results of the Viking atmospheric water detector experiment. J. Geophys. Res. 87, 2999–3019.

Kahre, M.A., Murphy, J.R., Haberle, R.M., 2006. Modeling the Martian dust cycle and surface dust reservoirs with the NASA Ames general circulation model. J. Geophys. Res. 111, E06008. https://doi.org/10.1029/2005JE002588.

Kalnay, E., 2003. Atmospheric Modelling, Data Assimilation and Predictability. Cambridge University Press.

Kaminski, J.W., Neary, L., Struzewska, J., McConnell, J.C., Lupu, A., Jarosz, J., Toyota, K., Gong, S.L., Côté, J., Liu, X., Chance, K., Richter, A., 2008. GEM-AQ, an on-line global multiscale chemical weather modelling system: model description and evaluation of gas phase chemistry processes, Atmos. Chem. Phys. 8, 3255–3281. https://doi.org/10.5194/acp-8-3255-2008.

Kaplan, L.D., Connes, J., Connes, P., 1969. Carbon monoxide in the Mars atmosphere. Astrophys. J. 157, L187–L192.

Kleinböhl, A., Schofield, J.T., Abdou, W.A., Irwin, P.G.J., de Kok, R.J., 2011. A singlescattering approximation for infrared radiative transfer in limb geometry in the Martian atmosphere. J. Quant. Spectrosc. Radiat. Transfer 112, 1568–1580. https://doi.org/10.1016/j.jqsrt.2011.03.006.

Korablev, O.I., Montmessin, F., Fedorova, A.A., Ignatiev, N.I., Shakun, A.V., Trokhimovskiy, A.V., Grigoriev, A.V., Anufreichik, K.A., Kozlova, T.O., 2015. ACS experiment for atmospheric studies on "ExoMars-2016" orbiter. Sol. Syst. Res. 49, 529–537. https://doi.org/10.1134/S003809461507014X.

Korablev, O.I., et al., 2018. The Atmospheric Chemistry Suite (ACS) of three spectrometers for the ExoMars 2016 Trace Gas Orbiter. Space Sci. Rev. 214, 7. https://doi.org/10.1007/s11214-017-0437-6.

Krasnopolsky, V.A., 1993. Photochemistry of the Martian atmosphere (mean conditions). Icarus 101, 313–332.

Krasnopolsky, V.A., Feldman, P.D., 2001. Detection of molecular hydrogen in the atmosphere of Mars. Science 294, 1914–1917.

Kuiper, G.P., 1949. Survey of planetary atmospheres. In: Kuiper, G.P. (Ed.), The Atmospheres of the Earth and Planets. Chicago Press, Chicago.

Lebonnois, S., Quémerais, E., Montmessin, F., Lefèvre, F., Perrier, S., Bertaux, J.-L., Forget, F., 2006. Vertical distribution of ozone on Mars as measured by SPICAM/Mars Express using stellar occultations. J. Geophys. Res. 111, E09S05. https://doi.org/10.1029/2005JE002643.

Lefèvre, F., Bertaux, J.-L., Clancy, R.T., Encrenaz, T., Fast, K., Forget, F., Lebonnois, S., Montmessin, F., Perrier, S., 2008. Heterogeneous chemistry in the atmosphere of Mars. Nature 454, 971–975. https://doi.org/10.1038/nature07116.

Lefèvre, F., Brasseur, G., Folkins, I., Smith, A.K., Simon, P., 1994. Chemistry of the 1991 – 1992 stratospheric winter: three-dimensional model simulations. J. Geophys. Res. 99, 8183–8195.

Lefèvre, F., Forget, F., 2009. Observed variations of methane on Mars unexplained by known atmospheric chemistry and physics. Nature 460, 720–723. https://doi.org/10.1038/nature08228.

Lefèvre, F., Krasnopolsky, V., 2017. Atmospheric photochemistry. In: Haberle, R.M., Clancy, R.T., Forget, F., Smith, M.D., Zurek, R.W. (Eds.), The Atmosphere and Climate of Mars, Cambridge University Press, pp. 405–432.

Lefèvre, F., Lebonnois, S., Montmessin, F., Forget, F., 2004. Three-dimensional modeling of ozone on Mars. J. Geophys. Res. 109, E07004. https://doi.org/10.1029/2004JE002268.

Lewis, S.R., Read, P.L., Conrath, B.J., Pearl, J.C., Smith, M.D., 2007. Assimilation of Thermal Emission Spectrometer atmospheric data during the Mars Global Surveyor aerobraking period. Icarus 192, 327–347.

Lian, Y., Richardson, M.I., Newman, C.E., Lee, C., Toigo, A.D., Mischna, M.A., Campin, Jean-Michel, 2012. The Ashima/MIT Mars GCM and argon in the martian atmosphere. Icarus 218, 1043–1070. https://doi.org/10.1016/j.icarus.2012.02.012.

Lindner, B.L., 1988. Ozone on Mars: the effects of clouds and airborne dust. Planet. Sp. Sci. 36 (2), 125–144.

Madeleine, J.-B., Forget, F., Millour, E., Navarro, T., Spiga, A., 2012. The influence of radiatively active water ice clouds on the Martian climate. Geophys. Res. Lett. 39, L23202. https://doi.org/10.1029/2012GL053564.

Mahaffy, P.R., Webster, C.R., Atreya, S.K., Franz, H., Wong, M., Conrad, P.G., Harpold, D., Jones, J.J., Leshin, L.A., Manning, H., Owen, T., Pepin, R.O., Squyres, S., Trainer, M., the MSL Science Team, 2013. Abundance and isotopic composition of gases in the Martian atmosphere from the Curiosity rover. Science 341, 263–266. https://doi.org/10.1126/science.1237961.

Maltagliati, L., Montmessin, F., Fedorova, A., Korablev, O., Forget, F., Bertaux, J.-L., 2011. Evidence of water vapor in excess of saturation in the atmosphere of mars. Science 333, 1868. https://doi.org/10.1126/science.1207957.

Maltagliati, L., Montmessin, F., Korablev, O., Fedorova, A., Forget, F., Määttänen, A., Lefèvre, F., Bertaux, J.-L., 2013. Annual survey of water vapor vertical distribution and water-aerosol coupling in the martian atmosphere observed by SPICAM/MEx solar occultations. Icarus 223, 942–962. https://doi.org/10.1016/j.icarus.2012.12.012.

McCleese, D.J., Schofield, J.T., Taylor, F.W., Calcutt, S.B., Foote, M.C., Kass, D.M., Leovy, C.B., Paige, D.A., Read, P.L., Zurek, R.W., 2007. Mars Climate Sounder: an investigation of thermal and water vapor structure, dust and condensate distributions in the atmosphere, and energy balance of the polar regions. J. Geophys. Res. 112, E05S06. https://doi.org/10.1029/2006JE002790.

McElroy, M.B., Donahue, T.M., 1972. Stability of the Martian atmosphere. Science 177, 986–988.

Montabone, L., Forget, F., Millour, E., Wilson, R.J., Lewis, S.R., Cantor, B., Kass, D., Kleinböhl, A., Lemmon, M.T., Smith, M.D., Wolff, M.J., 2015. Eight-year climatology of dust optical depth on Mars. Icarus 251, 65–95. https://doi.org/10.1016/j.icarus.2014.12.034.

Montmessin, F., Lefèvre, F., 2013. Transport-driven formation of a polar ozone layer on Mars. Nat. Geosci. 6, 930–933. https://doi.org/10.1038/ngeo1957.

Moreau, D., Esposito, L.W., Brasseur, G., 1991. The chemical composition of the dust-free Martian atmosphere: preliminary results of a two-dimensional model. J. Geophys. Res. 96, 7933–7945.

Moudden, Y., Forbes, J.M., 2008a. Effects of vertically propagating thermal tides on the mean structure and dynamics of Mars' lower thermosphere. Geophys. Res. Lett. 35, L23805. https://doi.org/10.1029/2008GL036086.

Moudden, Y., Forbes, J.M., 2008b. Topographic connections with density waves in Mars' aerobraking regime. J. Geophys. Res. 113, E11009. https://doi.org/10.1029/2008JE003107.

Moudden, Y., Forbes, J.M., 2014. Insight into the seasonal asymmetry of nonmigrating tides on Mars. Geophys. Res. Lett. 41, 2631–2636. https://doi.org/10.1002/2014GL059535.

Moudden, Y., Forbes, J.M., 2015. Density prediction in Mars' aerobraking region. Space Weather 13, 86–96. https://doi.org/10.1002/2014SW001121.

Moudden, Y., McConnell, J.C., 2005. A new model for multiscale modeling of the Martian atmosphere, GM3. J. Geophys. Res. 110, E04001. https://doi.org/10.1029/2004JE002354.

Moudden, Y., McConnell, J.C., 2007. Three-dimensional on-line chemical modeling in a Mars general circulation model. Icarus 188, 18–34. https://doi.org/10.1016/j.icarus.2006.11.005.

Mumma, M.J., Villanueva, G.L., Novak, R.E., Hewagama, T., Bonev, B.P., DiSanti, M.A., Mandell, A.M., Smith, M.D., 2009. Strong release of methane on Mars in northern summer 2003. Science 323, 1041–1045. https://doi.org/10.1126/science.1168980.

Musiolik, G., Kruss, M., Demirci, T., Schrinski, B., Teiser, J., Daerden, F., Smith, M.D., Neary, L., Wurm, G., 2018. Saltation under Martian gravity and its influence on the global dust distribution. Icarus 306, 25–31. https://doi.org/10.1016/j.icarus.2018.01.007.

Nair, H., Allen, M., Anbar, A.D., Yung, Y.L., 1994. A photochemical model of the Martian atmosphere. Icarus 111, 124–150.

Navarro, T., Forget, F., Millour, E., Greybush, S.J., 2014b. Detection of detached dust layers in the Martian atmosphere from their thermal signature using assimilation. Geophys. Res. Lett. 41, 6620–6626. https://doi.org/10.1002/2014GL061377.

Navarro, T., Madeleine, J.-B., Forget, F., Spiga, A., Millour, E., Montmessin, F., Määttänen, A., 2014a. Global climate modeling of the Martian water cycle with improved microphysics and radiatively active water ice clouds. J. of Geophys. Res. Planets 119, 1479–1495. https://doi.org/10.1002/2013JE004550.

Neary, L., Daerden, F., 2018. The GEM-Mars general circulation model for Mars: description and evaluation. Icarus 300, 458–476. https://doi.org/10.1016/j.icarus.2017.09.028.

Noxon, J.F., Traub, W.A., Carlton, N.P., Connes, P., 1976. Detection of O2 dayglow emission from Mars and the Martian ozone abundance. Astrophys. J. 207, 1025–1035.

Oehler, D., Etiope, G., 2017. Methane seepage on Mars: where to look and why. Astrobiology 17, 1233–1264. https://doi.org/10.1089/ast.2017.1657.

Owen, T., Biemann, K., Rushnek, D.R., et al., 1977. The composition of the atmosphere at the surface of Mars. J. Geophys. Res. 82, 4635–4639.

Parkinson, T.D., Hunten, D.M., 1972. Spectroscopy and aeronomy of O2 on Mars. J. Atmos. Sci. 29, 1380–1390.

Parkinson, W.H., Rufus, J., Yoshino, K., 2003. Absolute absorption cross section measurements of CO2 in the wavelength region 163–200 nm and the temperature dependence. Chem. Phys. 290, 251–256. https://doi.org/10.1016/S0301-0104(03)00146-0.

Perrier, S., Bertaux, J.L., Lefèvre, F., Lebonnois, S., Korablev, O., Fedorova, A., Montmessin, F., 2006. Global distribution of total ozone on Mars from SPICAM/MEX UV measurements. J. Geophys. Res. 111, E09S06. https://doi.org/10.1029/2006JE002681.

Robert, S., Camy-Peyret, C., Daerden, F., De Mazière, M., De Wachter, E., Neary, L., Vandenbussche, S., Vandaele, A.C., 2017. Two test-cases for synergistic detections in the Martian atmosphere: carbon monoxide and methane. J. Quant. Spectrosc. Radiat. Transf. 189, 86–104. https://doi.org/10.1016/j.jqsrt.2016.11.003.

Robert, S., Vandaele, A.C., Thomas, I., Willame, Y., Daerden, F., Delanoye, S., Depiesse, C., Drummond, R., Neefs, E., Neary, L., Ristic, B., Mason, J., Lopez-Moreno, J.-J., Rodriguez-Gomez, J., Patel, M.R., Bellucci, G., the NOMAD Team, 2016. Expected performances of the NOMAD/ExoMars instrument. Planetary and Space Science 124, 94–104. https://doi.org/10.1016/j.pss.2016.03.003.

Savijärvi, H., Määttänen, A., Kauhanen, J., Harri, A.-M., 2004. Mars Pathfinder: new data and new model simulations. Q. J. R. Meteorol. Soc. 130, 669–683.

Smith, M., Daerden, F., Neary, L., Khayat, S., 2018. The climatology of carbon monoxide and water vapor on Mars as observed by CRISM and modeled by the GEM-Mars general circulation model. Icarus 301, 117–131. https://doi.org/10.1016/j.icarus.2017.09.027.

Smith, M.D., 2004. Interannual variability in TES atmospheric observations of Mars during 1999–2003. Icarus 167, 148–165. https://doi.org/10.1016/j.icarus.2003.09.010.

Spiga, A., Hinson, D.P., Madeleine, J.-B., Navarro, T., Millour, E., Forget, F., Montmessin, F., 2017. Snow precipitation on Mars driven by cloud-induced night-time convection. Nat. Geosci. 10, 652–657. https://doi.org/10.1038/NGEO3008.

Spinrad, H., Munch, G., Kaplan, L.D., 1963. The detection of water vapor on Mars. Astrophys. J. 137, 1319–1321.

Steele, L.J., Lewis, S.R., Patel, M.R., 2014a. The radiative impact of water ice clouds from a reanalysis of Mars Climate Sounder data. Geophys. Res. Lett. 41, 4471–4478. https://doi.org/10.1002/2014GL060235.

Steele, L.J., Lewis, S.R., Patel, M.R., Montmessin, F., Forget, F., Smith, M.D., 2014b. The seasonal cycle of water vapour on Mars from assimilation of Thermal Emission Spectrometer data. Icarus 237, 97–115. https://doi.org/10.1016/j.icarus.2014.04.017.

Summers, M.E., Lieb, B.J., Chapman, E., Yung, Y.L., 2002. Atmospheric biomarkers of subsurface life on Mars. Geophys. Res. Lett. 29, 2171. https://doi.org/10.1029/2002GL015377.

Talagrand, O., 1997. Assimilation of observations, an introduction. J. Met. Soc. Japan 75 (1B), 191–209.

Trokhimovskiy, A., Fedorova, A., Korablev, O., Montmessin, F., Bertaux, J.-L., Rodin, A., Smith, M.D., 2015. Mars' water vapor mapping by the SPICAM IR spectrometer: five Martian years of observations. Icarus 251, 50–64.

Vandaele, A.C., et al., 2015. Science objectives and performances of NOMAD, a spectrometer suite for the ExoMars TGO mission. Planetary and Space Science 119, 233–249. https://doi.org/10.1016/j.pss.2015.10.003.

Vandaele, A.C., et al., 2018. NOMAD, an integrated suite of three spectrometers for the ExoMars Trace Gas Mission: technical description, science objectives and expected performance. Space Sci. Rev. 214, 80. https://doi.org/10.1007/s11214-018-0517-2.

Venot, O., Bénilan, Y., Fray, N., Gazeau, M.-C., Lefèvre, F., Es-sebbar, Et., Hébrard, E., Schwell, M., Bahrini, C., Montmessin, F., Lefèvre, M., Waldmann, I.P., 2018. VUV-absorption cross section of carbon dioxide from 150 to 800 K and applications to warm exoplanetary atmospheres. Astron. Astrophys. 609, A34. https://doi.org/10.1051/0004-6361/201731295.

Villanueva, G.L., et al., 2015. Strong water isotopic anomalies in the martian atmosphere: probing current and ancient reservoirs. Science 348, 218. https://doi.org/10.1126/science.aaa3630.

Viscardy, S., Daerden, F., Neary, L., 2016. Formation of layers of methane in the atmosphere of Mars after surface release. Geophys. Res. Lett. 43 (5), 1868–1875. https://doi.org/10.1002/2015GL067443.

Webster, C.R., et al., 2015. Mars methane detection and variability at Gale crater. Science 347, 415–417. https://doi.org/10.1126/science.1261713.

Webster, C.R., et al., 2018. Background levels of methane in Mars' atmosphere show strong seasonal variations. Science 360 (6393), 1093–1096. https://doi.org/10.1126/science.aaq0131.

Wu, D., 2015. Modeling the dust cycle on Mars with the Global Mars Multiscale Model GEM-Mars, PhD thesis. In: York Univ. Toronto, Canada.

Yeh, K.-S., Côté, J., Gravel, S., Méthot, A., Patoine, A., Roch, M., Staniforth, A., 2002. The CMC-MRB Global Environmental Multiscale (GEM) Model. Part III: Nonhydrostatic Formulation. Mon. Wea. Rev. 130, 339–356.

Zahnle, K., Freedman, R.S., Catling, D.C., 2011. Is there methane on Mars? Icarus 212, 493503. https://doi.org/10.1016/j.icarus.2010.11.027.

Zurek, R.W., Chicarro, A., Allen, M.A., Bertaux, J.-L., Clancy, R.T., Daerden, F., Formisano, V., Garvin, J.B., Neukum, G., Smith, M.D., 2011. Assessment of a 2016 mission concept: the search for trace gases in the atmosphere of Mars. Planet. Sp. Sci. 59, 284–291. https://doi.org/10.1016/j.pss.2010.07.007.